



HAL
open science

Experimental and numerical investigation of gas-side mass transfer in Taylor flow

Emilien Bourdon, Carine Julcour-Lebigue, Anne-Marie Billet, David Rouzineau, Céline Volpi, Renaud Cadours

► **To cite this version:**

Emilien Bourdon, Carine Julcour-Lebigue, Anne-Marie Billet, David Rouzineau, Céline Volpi, et al.. Experimental and numerical investigation of gas-side mass transfer in Taylor flow. Separation and Purification Technology, 2023, 315, pp.123599. 10.1016/j.seppur.2023.123599 . hal-04193157

HAL Id: hal-04193157

<https://hal.science/hal-04193157>

Submitted on 4 Sep 2023

HAL is a multi-disciplinary open access archive for the deposit and dissemination of scientific research documents, whether they are published or not. The documents may come from teaching and research institutions in France or abroad, or from public or private research centers.

L'archive ouverte pluridisciplinaire **HAL**, est destinée au dépôt et à la diffusion de documents scientifiques de niveau recherche, publiés ou non, émanant des établissements d'enseignement et de recherche français ou étrangers, des laboratoires publics ou privés.

Journal Pre-proofs

Experimental and numerical investigation of gas-side mass transfer in Taylor flow

BOURDON Emilien, JULCOUR Carine, BILLET Anne-Marie,
ROUZINEAU David, VOLPI Céline, CADOURS Renaud

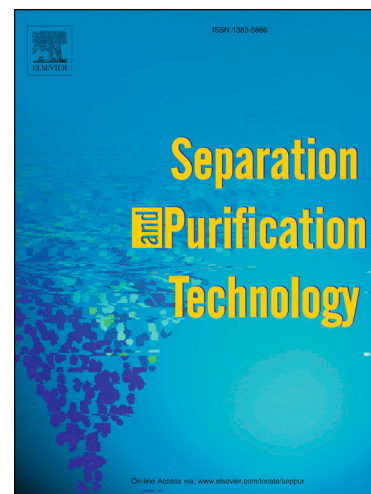
PII: S1383-5866(23)00507-5
DOI: <https://doi.org/10.1016/j.seppur.2023.123599>
Reference: SEPPUR 123599

To appear in: *Separation and Purification Technology*

Received Date: 6 January 2023
Revised Date: 8 March 2023
Accepted Date: 10 March 2023

Please cite this article as: B. Emilien, J. Carine, B. Anne-Marie, R. David, V. Céline, C. Renaud, Experimental and numerical investigation of gas-side mass transfer in Taylor flow, *Separation and Purification Technology* (2023), doi: <https://doi.org/10.1016/j.seppur.2023.123599>

This is a PDF file of an article that has undergone enhancements after acceptance, such as the addition of a cover page and metadata, and formatting for readability, but it is not yet the definitive version of record. This version will undergo additional copyediting, typesetting and review before it is published in its final form, but we are providing this version to give early visibility of the article. Please note that, during the production process, errors may be discovered which could affect the content, and all legal disclaimers that apply to the journal pertain.



Experimental and numerical investigation of gas-side mass transfer in Taylor flow

BOURDON Emilien^{1,2}, JULCOUR Carine¹, BILLET Anne-Marie¹, ROUZINEAU David¹, VOLPI Céline², CADOURS Renaud²

¹ Laboratoire de Génie Chimique, Université de Toulouse, UMR 5503, CNRS, INPT, UPS, 4 Allée Émile Monso, 31 030, Toulouse, France

² TotalEnergies SE, 2 Place Jean Millier, 92 078, Paris La Défense Cedex, France

Corresponding author: JULCOUR Carine

Mail address: julcour.carine@toulouse-inp.fr

Postale address: Laboratoire de Génie Chimique, Université de Toulouse, UMR 5503, CNRS, INPT, UPS, 4 Allée Émile Monso, 31 030, Toulouse, France

Keywords: mass transfer, Taylor flow, solvent vaporization, image processing, direct numerical simulation

Abstract:

Taylor flows are of great interest for industrial application where efficient gas absorption is needed. Literature however scarcely relates to the gas-side mass transfer coefficient k_G in Taylor flows. In this work, the authors selected and developed an experimental method, based on bubble expansion record, to estimate k_G value in a millimetric channel of circular section, fed with nitrogen gas and pure ethyl acetate (*EA*). The experiments provided an order of magnitude of a few $\text{mm}\cdot\text{s}^{-1}$ at least for k_G , for a two-phase velocity $U_{TP} \sim 0.1 \text{ m}\cdot\text{s}^{-1}$.

CFD simulations completed the experimental investigation and further estimated the order of magnitude, with $k_G \sim 10^{-2} \text{ m}\cdot\text{s}^{-1}$ when $0.09 < U_{TP} < 0.18 \text{ m}\cdot\text{s}^{-1}$. The transport of *EA* inside the bubble suggests a significant contribution of diffusion in regard with the convective effects. k_G is found to be sensitive to U_{TP} , and to the temperature *via* the gas diffusivity and also *via* the bubble expansion leading to an increase in bubble velocity. The dependence of the gas-side Sherwood number to the Péclet number is similar to previously reported observations concerning a spherical bubble freely rising in quiescent liquid.

This study thus provides the means to evaluate the gas-side resistance for any gas-liquid system in Taylor flows, a resistance that was usually simply dismissed in previous works. As an example, the authors demonstrated that, in Taylor flows, for a gas-liquid system of industrial interest (diluted CO_2 in 30 wt.% N-methyldiethanolamine aqueous solution), gas-side mass transfer resistance is lower than the liquid-side one by at least one order of magnitude.

1 Introduction

1.1 Context and objectives of the study

Since the 90's, micro- or milli-structured devices have often been considered for a range of possible applications in process engineering, where mass or heat transfer in a gas-liquid system is needed. In these contactors, several flow regimes can be observed, depending on the gas and liquid flow rates. Milli-channel reactors operating in the Taylor flow regime represent a particularly interesting option in this respect. This flow regime shows a periodic pattern consisting in a continuous train of bubbles separated by liquid slugs. Amongst its benefits, one can mention a moderate pressure drop, a high contact area between phases, and a strong liquid recirculation within the liquid slugs, giving rise to

nearly plug flow behavior [1, 2, 3, 4]. This recirculation, together with the presence of a thin lubrication film between bubbles and channel wall, and with the large achievable surface-to-volume ratio, intensify gas-liquid mass transfer efficiency: Taylor flow leads to gas-liquid volumetric mass transfer coefficient $k_L a$ as high as 1.6 s^{-1} [5]. Thus, cutting-edge technologies of milli-structured reactors have been investigated for some 30 years, as monolith reactors, for mass transfer limited gas-liquid reactions [6, 7]. If needed, catalyst can be deposited on channel wall in a layer of 10-30 μm . Similarly, gas cleaning processes are considered in thin channels [8, 9, 10, 11].

To conceive and design gas-liquid technologies, reliable upscaling laws are needed to estimate mass transfer efficiency. The absorption rate of gases in liquids depends on the gas-side and liquid-side resistances. Literature offers several experimental or numerical studies about liquid-side mass transfer coefficient k_L (or $k_L a$) in Taylor flow [5, 12, 13, 14, 15, 16, 17, 18]. However, concerning gas-side mass transfer coefficient in segmented flow, data are scarce.

Gas-side resistance is usually assumed to be negligible in regard with liquid-side one [12, 14, 16, 17, 19, 20], even though, for gas mixtures and components showing a high solubility in the liquid phase, and/or involved in a fast chemical reaction in the liquid phase - as CO_2 in aqueous sodium hydroxide (NaOH) solutions, this hypothesis may be wrong and needs to be verified.

In this work, the authors investigate through both experimental and numerical approaches the gas-side mass transfer resistance in Taylor flow under determined conditions in which it may impact the overall mass transfer rate.

1.2 State of the art: gas-side mass transfer investigation

1.2.1 Mass transfer limitations

Within transferring gas-liquid systems, in the vicinity of each side of the interface, thin layers of concentration gradient exist, where mass transfer resistance takes place. The simplest model - and the easiest to use - is the two-film model proposed by Lewis and Whitman in 1924 [21]. To estimate the relative importance of gas-side mass transfer, it is recalled that the overall resistance to mass transfer between the two phases is the sum of the resistances from each side of the interface:

For physical absorption:

$$\frac{1}{K_{GL}} = \frac{1}{k_L} + \frac{H \cdot R \cdot T}{k_G} \quad (1)$$

For reacting systems:

$$\frac{1}{K_{GL}} = \frac{1}{E \cdot k_L} + \frac{H \cdot R \cdot T}{k_G} \quad (2)$$

In these equations, H is the Henry's constant (standing for the solute gas solubility) in $\text{mol} \cdot \text{m}^{-3} \cdot \text{Pa}^{-1}$, T the temperature (K), R the universal gas constant ($\text{J} \cdot \text{K}^{-1} \cdot \text{mol}^{-1}$), k_L and k_G the liquid-side and gas-side mass transfer coefficients, respectively ($\text{m} \cdot \text{s}^{-1}$), K_{GL} the overall mass transfer coefficient ($\text{m} \cdot \text{s}^{-1}$) and E the mass transfer enhancement factor (dimensionless) due to the chemical reaction in the liquid phase.

The mass transfer coefficients obey to:

$$N_A = k_G(C^G - C^{G,i}) = k_L(C^{L,i} - C^L) \quad (3)$$

where N_A is the solute mass transfer flow rate per unit interfacial area ($\text{mol} \cdot \text{m}^{-2} \cdot \text{s}^{-1}$), C^G is the solute concentration in the bubble, C^L the solute concentration in the bulk liquid phase, and $C^{G,i}$ and $C^{L,i}$ the solute concentration each side of the interface (concentrations in $\text{mol} \cdot \text{m}^{-3}$ of the considered phase). Equation (3) implies that the determination of each mass transfer coefficient would require the

measurement of the interfacial and bulk concentrations of the solute. However, even recent experimental techniques cannot reach local concentration close enough to the interface. The individual film coefficients can thus only be accurately determined under experimental conditions where mass transfer resistance on one side can be neglected.

1.2.2 Measurement techniques for gas-side mass transfer investigation

Gas cleaning operations have developed since the beginning of the 20th century. Thus, in the 40's, a large number of authors have focused on the evaluation of the volumetric mass transfer coefficients $k_L a$ and $k_G a$, and also on the available interfacial area a in various contactors.

In a recent review, Hegely and his collaborators [22] collected and compared measurement approaches for mass transfer coefficients and interfacial area in packing columns. They described the equipments and operating procedures and discussed the experimental accuracy. Values of k_G and k_L are generally obtained by dividing $k_G a$ by the specific interfacial area a , which is issued from separate measurements. Errors in a then propagate into the mass transfer coefficients.

To obtain the value of k_G , the liquid-side mass transfer resistance has to be negligible or known. In theory, the liquid-side mass transfer resistance is negligible only if the liquid phase is purely the solute, *i.e.* there is no concentration gradient on liquid side. In all other cases, the contribution of the liquid-side resistance has to be assessed.

The methods for investigating k_G can be classified into three groups related to the principle of the measurement:

(i) Vaporization of a pure liquid:

The mass transfer driving force stands in the gas phase near the interface and involves the equilibrium concentration of the liquid specie in the gas phase. The equilibrium temperature is assumed to be that of the liquid. The accuracy of the temperature measurement is thus crucial: Hegely and co-workers [22] claim that, for experiment performed at 293 K with water, a 1 K error induces a 6% change in the vapor pressure. If the system operates within 20% of saturation, the $k_G a$ value will show 30% uncertainty. The liquid temperature must be stable too, within 0.2 K [22], to minimize the heat transfer in the liquid phase. Note that the reverse process - dehumidification or condensation - may also be a method to measure $k_G a$.

(ii) Physical absorption (or desorption):

This strategy consists in using a solute whose solubility in the liquid is high enough to minimize liquid-side resistance. For instance, if the liquid phase is water, the gaz phase may be acetone, ammonia or methanol in air. However, the liquid-side resistance cannot be fully negligible, and has to be quantified in order to determine $k_G a$.

(iii) Chemical absorption:

The liquid-side resistance can be strongly reduced if a chemical reaction consumes the solute and if its rate is high enough to eliminate the solute from the liquid film near the interface. Typically, a basic aqueous solution, such as NH_3 or $NaOH$, is used to absorb an acidic solute, such as H_2S , SO_2 , or CO_2 .

1.2.3 Gas-side mass transfer coefficient for conventional gas-liquid technologies

Based on these measurement methods, many empirical correlations have been published for these parameters relating them to the operating conditions, type of contactor, packing geometry, and physical properties of the phases.

Vidwans and Sharma [23] reviewed the first established correlations for $k_G a$ in packed columns, and also provided their own measurements with Raschig rings and Intalox saddles, based on the absorption of a dilute gas with fast reaction on liquid side. These authors varied the gas and liquid flow rates and used solute gases with contrasted solubilities. They observed that the correlations for $k_G a$ did not always agree with respect to the dependence on gas diffusivity or Schmidt number. These discrepancies ensue the various experimental methods applied to various apparatus, and evidence that these methods need a cautious evaluation. Roustan [24] provided for k_G orders of magnitude of 0.03 to 0.07 m.s⁻¹ in random packed columns (depending on the studied gas-liquid system). Razi and colleagues [25] compared the predictions of correlations for structured packings, which resulted in k_G values varying from 0.01 to 0.08 m.s⁻¹ for absorption of CO_2 from flue gas in Monoethanolamine (MEA) solution.

Gas-side coefficient has been investigated in *bubble columns* too. For instance, Cho and Wakao [26] measured the overall coefficient $K_{GL} a$ in a pilot column. They used aqueous solutions containing a dilute organic solute, which was stripped by nitrogen bubbles. The six chosen organic solutes show contrasted solubilities in water. The authors measured the time evolution of the solute concentration in the liquid phase and gathered the results in a plot of $1/K_{GL} a$ versus $(H \cdot R \cdot T)$. They then obtained a straight-line whose origin ordinate is $1/k_L a$ and whose slope is $1/k_G a$. They inferred $k_G a$ values between 0.1 and 1 s⁻¹. They derived a correlation for $k_G a$, which is valid in bubble column for a single nozzle and (with a different multiplying constant) for a bundle of three porous tubes. This correlation shows that, as for packings [23], $k_G a$ is related to the square root of the solute diffusivity in the gas phase (in an analogous way to $k_L a$ which is related to the square root of the solute diffusivity in the liquid phase).

It may be interesting to relate these experimental values to the theoretical gas-side coefficient for a single spherical bubble rising in a quiescent liquid, as determined by direct numerical simulations [27]. For Reynolds numbers (related to the bubble diameter and velocity) ranging from 0.1 to 100, the authors show that the asymptotic value of the gas-side Sherwood number (obtained when $t \rightarrow \infty$) reaches a maximum value of 18 at very high Péclet number, assessing previous numerical and analytical works. For a 2 mm bubble containing CO_2 in nitrogen and slowly rising in water at 293 K, this corresponds to $k_G \sim 0.14$ m.s⁻¹. Note that, for a motionless bubble, the asymptotic Sherwood number stands around 6.5.

1.2.4 Gas-side mass transfer in Taylor flow

As mentioned, the evaluation of the gas-liquid mass transfer coefficient in Taylor flow has been the subject of a wide number of articles. However, it is observed that the proposed correlations for the liquid-side coefficient can lead to contrasted values, differing by up to one order of magnitude [5], due to the complex feature of mass transfer in this type of flow. Very few works (mentioned here after) focus on k_G measurement in Taylor flow, either for micro- or milli-channels, and even for fast reactions and gas mixtures. *A fortiori*, to the authors' knowledge, the spatial evolution of k_G along the channel in Taylor flow has never been studied. As mentioned in section 1.1, many experimental works dedicated to gas-liquid mass transfer in slug flow assume that the gas phase resistance is negligible, even though the gas species to be transferred is mixed with other species in the gas phase. However, some authors estimate the $k_G a$ contribution within the overall mass transfer coefficients via numerical calculations.

Shao and colleagues [28] modelled the transfer of CO_2 from a gas mixture (5% vol. CO_2 in N_2) into an aqueous $NaOH$ solution, considering that the phenomenon on gas side is purely diffusive. They observed weak concentration gradients in the gas phase for either physical mass transfer and reactive absorption. Sobieszuk and collaborators [29] modelled these phenomena in a 0.4 mm diameter channel by use of the numerical tool COMSOL®. They also concluded that depending on the solute gas solubility, the liquid-side resistance is not always the major one. For instance, in the case of physical absorption of a poorly soluble solute ($H < 10^{-2} \text{ mol}\cdot\text{m}^{-3}\cdot\text{Pa}^{-1}$), liquid-side mass transfer resistance is prevailing. However, when a fast chemical reaction takes place in the liquid phase, the liquid-side resistance decreases when the enhancement factor increases: the gas-side resistance may not be always negligible for gases of medium to high solubility ($H > 10^{-4} \text{ mol}\cdot\text{m}^{-3}\cdot\text{Pa}^{-1}$) over the classical range of E values – between 1 and 100 [21].

For Taylor flows, it is then not possible to state that one of the mass transfer resistances prevails. Detailed investigations have to be performed.

1.3 Adopted approach

Among the experimental methods reported above, the vaporization of a pure liquid has been preferred because it ensures that there is no liquid-side resistance. The method only requires knowing the vapour pressure of the chosen liquid, but no kinetic law nor solubility data in liquid are needed.

In this work, experiments are performed using nitrogen gas and pure organic liquid in Taylor flow in a single channel of 2 mm of inner diameter and 1 m of length. For several experiments (stable Taylor flows at various flowrates and temperatures), images of bubbles are recorded along the channel thanks to a high-speed camera, far enough to the channel inlet and outlet as to avoid flow disturbance. Bubble size is determined thanks to the shadowgraphy technique and to image analysis. A 1-D model is developed with MATLAB® which relates local bubble size in the channel to the local solute concentration and total pressure. Thanks to this model, the comparison of the measured bubble size with the calculated ones allows identifying the coefficient k_G .

The objective is to sort out the question of the gas-side mass transfer significance by determining its order of magnitude, and to investigate its sensitivity to the hydrodynamic characteristics of the flow. Thus, numerical simulations are performed to describe and analyze the phenomena at bubble scale, to assess the trends and order of magnitude observed for the experimental values of k_G , and to investigate its sensitivity to parameters outside of the experimental operating envelope (e.g. temperature, flow velocity and solute diffusivity). These issues are discussed in detail in the following sections.

2 Experimental set-up and procedures

2.1 Fluids selection

For the experiments, an inert gas and a volatile solvent are needed. Nitrogen is selected, as poorly soluble in liquids. To measure bubble size via the shadowgraphy technique with satisfactory accuracy, bubble volume must grow along the channel with more than 10% of relative variation. At atmospheric pressure, the solvent vapour pressure shall then be higher than 10,000 Pascal. However, temperature control is difficult as heat losses at channel inlet and outlet cannot be fully avoided. As a consequence, experiments are performed at moderate temperature (293 K – 323 K). In this range, solvent with sufficient vapour pressures have been considered: chloroform, methanol, benzene, methyl acetate, diethyl ether, acetone, ethyl acetate and ethanol. Most of them have been dismissed because of their toxicity or possible interaction with the pilot seals. Ethyl acetate (EA) is chosen. Thermodynamic

equilibrium at atmospheric pressure shows 10% of ethyl acetate in nitrogen gas at 293 K, and 38% at 323 K.

Antoine's law used in this work to calculate the ethyl acetate vapour pressure is given by equation (4), which uses the coefficients recommended by [30]:

$$\log_{10}(P_{EA}^{vap}) = 4.22809 - \frac{1245.702}{T - 55.189} \quad (4)$$

with P_{EA}^{vap} in bar and T in K.

Useful physico-chemical properties of *EA* and nitrogen are gathered in Table 1.

Temperature (K)	ρ (kg.m ⁻³)		μ (Pa.s)		σ (N.m ⁻¹)
	<i>EA</i> (liquid)	<i>N</i> ₂ (gas)	<i>EA</i> (liquid)	<i>N</i> ₂ (gas)	
293	897	1.16	$4.27 \cdot 10^{-4}$	$1.75 \cdot 10^{-5}$	$2.36 \cdot 10^{-2}$
323	863	1.06	$2.04 \cdot 10^{-4}$	$1.90 \cdot 10^{-5}$	$2.04 \cdot 10^{-2}$

Table 1. Physico-chemical properties of ethyl acetate and nitrogen under atmospheric pressure. "EA" stands for ethyl acetate.

2.2 Single channel setup

The experimental set-up (Figure 1) consists in a vertical cylindrical capillary glass tube made with 2 ± 0.01 mm internal diameter and 1 m length. The liquid (ethyl acetate, >99%, Acros Organics™, Fisher Scientific S.A.S., France) is circulated into the channel from a reservoir tank (mixed and saturated by bubbling nitrogen) using a gear pump (Tuthill D-series, Bronkhorst® France) controlled by a Coriolis mass flow instrument (Bronkhorst® France, mini-CORI FLOW™, 0-15 kg.h⁻¹).

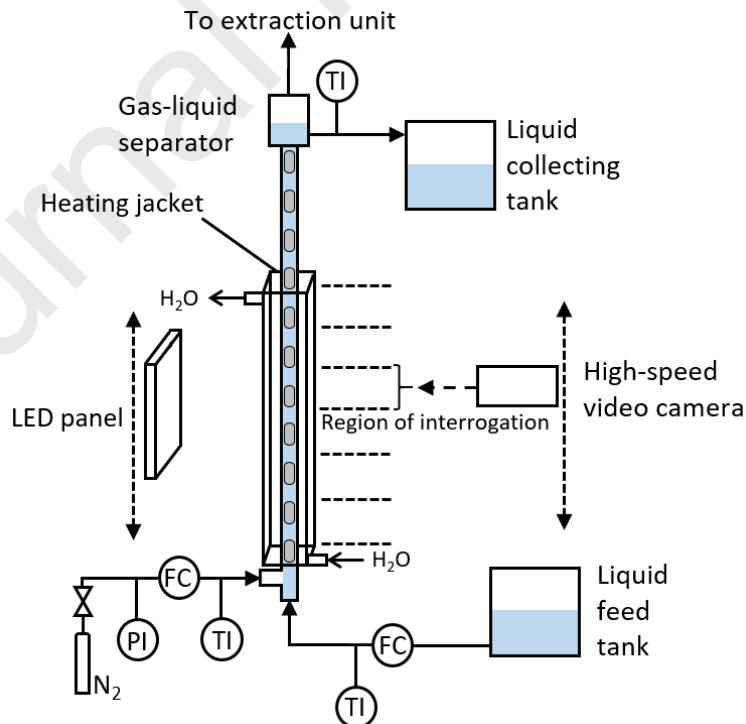


Figure 1. Scheme of the experimental single channel set-up.

The gas supplied from a N_2 gas cylinder (4.5 grade: >99,995%, Linde Gas, Linde France S.A.) is regulated at 1.2 bara and a thermal mass flow controller (Brooks SLA5850S, 0-15 normal liters per hour (NL.h⁻¹)) adjusts its flow rate. The two phases are contacted through a T-junction embedded in a Teflon piece before entering the single channel in upflow mode. They are disengaged in a gas-liquid separator made of Teflon: the gas is vented to an extraction unit, while the liquid phase is stored in a separate tank. A 0.6 m long cylindrical jacket made of transparent methyl metacrylate insures temperature control in the channel. In this jacket, water circulates in co-current mode, the temperature of which is regulated at the desired value. Heating strings are placed around channel inlet and outlet and regulated at the desired temperature to minimize heat losses. Pt100 probes are located on the liquid line before the gas-liquid injector and after the gas-liquid separator.

2.3 Shadowgraphy equipment

Shadowgraphy images were acquired by a high-speed sCMOS camera (PCO Edge 5.5, Photon Lines SAS) with a resolution of 2560x402 px². The camera was equipped with a 105 mm f/2.8 Nikon lens. Several regions of interrogation (ROI) were investigated along the channel. Each of them was 10 cm long to insure to catch a significant bubble size increase. This led to spatial definition of 40 $\mu\text{m}\cdot\text{px}^{-1}$ in the axial direction. The lowest ROI started 9 cm above the T-junction. A LED panel (Phlox[®], 20 x 20 cm², continuous light source, Phlox Corp, France) was settled behind the channel and lighted the ROI. A stand allowed moving the camera vertically along the circular double jacket. The camera and the LED panel were set at the middle of the considered interrogation area.

2.4 Experimental procedure and selected operating conditions

For each experiment, the tube was initially fed with gas, and then with liquid to prevent liquid entering the gas line. The temperature was set to 293 K or to 323 K, to limit the heat losses and to fulfill an observable bubble size growth along the visualization zone. The two phases flowed at the desired temperature and left the channel at atmospheric pressure. Prior to the experiments, a dedicated study was performed to check the flow regimes obtained with different flow rates of nitrogen and ethyl acetate. The gas flow rate was then set in the range [0.4-6.8] NL.h⁻¹, and the liquid one in the range [0.4-1.13] L.h⁻¹ to ensure the Taylor flow regime. The flow was recorded over a long time (up to 4 hours) to check for its stability. A sequence of 4,000 frames was then taken for each ROI, which corresponds to recording durations of 33 to 40 s. Note that 3,000 frames were usually large enough to reach converged time-averaged values of the deduced bubble features, and that the experiments which did not fulfill this criterion after 4,000 images were rejected. The acquisition frequency and exposure time were set between 100 and 120 Hz and between 1 and 2 ms, respectively, depending on the flow conditions. These values allowed capturing the gas-liquid flow features and getting precise bubble images.

In a preliminary study, the various flow regimes observed in the channel were determined for the system N_2 —EA at 293 K and 323 K, when varying gas and liquid flow rates. This led to the selected operating conditions (Table 2). The latter allow estimating, for the inlet conditions, the meaningful non-dimensional numbers for Taylor flow: the Capillary number ($Ca = \frac{\mu_L \cdot U_B}{\sigma_L}$), the Weber number ($We = \frac{\rho_L \cdot U_B^2 \cdot d_c}{\sigma_L}$) and the bubble Reynolds number ($Re_B = \frac{\rho_L \cdot U_B \cdot d_B}{\mu_L}$), where U_B is the bubble velocity along the channel.

The flow regime was laminar in the liquid slug, since Re_B was low (<1200). Ca values varied between $0.9 \cdot 10^{-3}$ and $2 \cdot 10^{-3}$, showing the predominance of surface tension effects over viscous force, and We values ranged between 0.6 and 1.5, so inertial effects were not significant in the experiments. Therefore, bubbles exhibited the “ideal” shape [5]: a cylindrical body with two half-spheres added.

Case N°	T_{EA}^{in} (K)	T_{jacket}^{in} (K)	T_{jacket}^{out} (K)	Number of recorded series	$Q_{N_2}^G$ (NL.h ⁻¹)	Q_{EA}^L (L.h ⁻¹)	f_{acq} (Hz)	$P_{t,0}$ (bar)
1	298.3	295.4	291.1	15	0.5	0.5	100	1.06
2	324.7	322.2	321.4	10	0.5	0.5	100	1.06
3	323.9	322.2	321.5	10	0.5	0.5	100	1.06
4	293.3	- *	- *	11	0.5	0.5	120	1.07
5	324.1	322.1	321.3	11	0.5	0.5	120	1.06
6	322.6	322.2	321.4	8	0.75	0.75	120	1.06

Table 2. Summary of investigated conditions.

* No circulation in the double jacket for this experiment.

2.5 Image processing

The Image Processing Toolbox of MATLAB® R2019.a was used to monitor the recorded images and to extract bubble features. The procedure is well-known (see for example [18]) and consisted in steps of binarization of bubble images, bubble labelling, calculation of bubble features (volume, surface area, velocity) according to their location, which are briefly described below.

Binarization of the bubble images

Before any processing, the 8-bit grayscale images were converted into 64-bit images. A ‘blank image’ of the liquid-filled channel (without bubble) was created from all bubble images of the sequence by retaining only the brightest pixels from one image to the other. This ‘blank image’ was subtracted from the bubble image to remove the channel wall. The image contrast was enhanced before transformation of the grayscale image into binary image using an automatic thresholding. The contour of the bubbles was smoothed by removing isolated pixels and performing morphological operations (e.g. closing operation). The interior area of the bubbles was filled by setting the interior pixels to “1” value.

Bubble labelling and calculation of bubble features

Each ROI of the channel showed from 10 to 18 bubbles on one single image, depending on the flow conditions. On each binarized ROI image, “objects” (bubbles) were detected thanks to preprogrammed MATLAB® function, and the image was split into interrogation areas (IA) of unit cell size (each IA contains one bubble). Depending on the position of these IA in the ROI, bubbles, when complete, were labelled “1”, “2” ... “n”, from left to right (Figure 2), i.e. in the direction of bubble motion. For each IA “i”, image analysis allowed the determination of bubble length (L_B), and of mass center location, using adapted MATLAB® functions. It is important to note that, the channel being surrounded by the water-filled circular double jacket, images of the flow suffered from optical distortion in the radial direction. So, it was not intended to extract directly bubble volumes from the images, but bubble lengths only, as this parameter was obtained on channel axis without any distortion. The volume and surface (V_B and S_B , respectively) were then computed for each bubble under the assumption of ideal shape. Finally, for each IA, the time-averaged position of its center was calculated and stored, and bubble lengths were time averaged. The respective maximum relative deviations on these averages are 25% on the position of the center and 10% on L_B .

For all operations from binarization, the processing of 4,000 images needed a total CPU time of ~60 minutes on a laptop computer running 64-bit Windows 10 with Intel Core i7 8850H@2.6-4.3 GHz and 64 Gb-RAM.

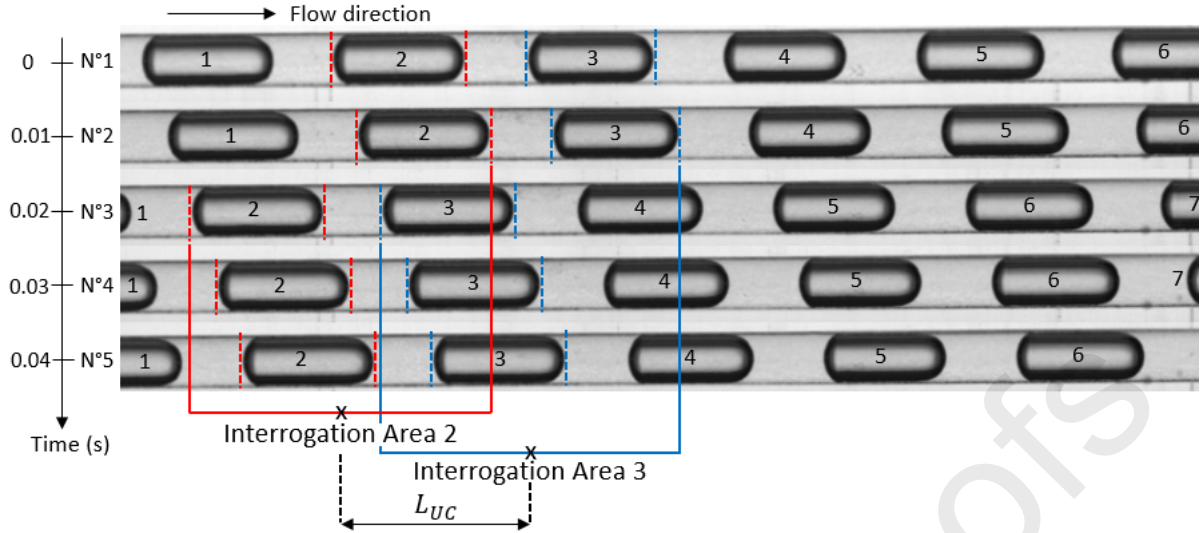


Figure 2. Illustration on grayscale images of the series of labelled Interrogation Areas, as defined in the ROI, and of their evolution in time. About half of the ROI is shown here. Experiment performed at $T = 293$ K, acquisition frequency: 100 Hz.

3 Evaluation of the local gas-side mass transfer coefficient k_G

3.1 1-D model for gas-side mass transfer in Taylor flow

In this section, the gas-side coefficient k_G is related to the time evolution of bubble size during the journey of the unit cell along the channel, with the aim to identify the value of k_G through the comparison of modelled and measured bubble sizes. So, in the model, all parameters are deduced either from known information at channel entrance (gas and liquid flow rates, pressure) or from a reference bubble size, as measured close to channel end. This is detailed here after.

3.1.1 Model background and founding equations

Temperature is considered uniform in the entire zone where the double jacket surrounds the channel. Bubble diameter (d_B) is assumed constant along the channel, since bubble velocity variation is small enough to neglect the variation of Capillary number (and thus that of the lubrication film thickness). Since the solubility of nitrogen in ethyl acetate (EA) is negligible, total pressure variation and EA vaporization are the only phenomena affecting bubble length (L_B). To model the evolution of L_B along the channel, a balance in EA is applied to a current unit cell:

$$N_{EA}^G = k_G (C_{EA}^{G,i} - C_{EA}^G) \quad (5)$$

where N_{EA}^G is the molar flow rate of transferred EA per unit interfacial area, $C_{EA}^{G,i}$ is the concentration in EA at interface (gas-side), and C_{EA}^G is the bulk concentration in EA inside the bubble.

EA being pure in this work, $C_{EA}^{G,i} = C_{EA}^{G,*}$, where $C_{EA}^{G,*}$ is the gas-phase EA concentration in equilibrium with the bulk liquid-phase EA concentration.

The gas phase being composed mainly of nitrogen, and used at moderate pressure and temperature, ideal gas law applies, and $C_{EA}^{G,*}$ can be expressed as:

$$C_{EA}^{G,*} = \frac{P_{EA}^{vap}}{R \cdot T} \quad (6)$$

where P_{EA}^{vap} is the EA saturation vapour pressure. The transferred EA rate is then written:

$$N_{EA}^G = \frac{k_G}{R \cdot T} (P_{EA}^{vap} - P_{EA}) \quad (7)$$

In the considered unit cell, the time evolution of the number of EA moles in the bubbles is:

$$\frac{dn_{EA}^G}{dt} = N_{EA}^G \cdot S_B = \frac{k_G \cdot S_B}{R \cdot T} (P_{EA}^{vap} - P_{EA}) \quad (8)$$

and can be expressed in terms of the total number of gas moles in the bubble (as nitrogen transfer is neglected):

$$\frac{dn_{EA}^G}{dt} = \frac{1}{R \cdot T} \cdot \frac{d}{dt} (P_t \cdot V_B) \quad (9)$$

Taking bubble shape in account, bubble volume V_B and bubble surface S_B are defined as:

$$V_B = (L_B - d_B) \frac{\pi d_B^2}{4} + \frac{\pi}{6} d_B^3 \quad (10)$$

$$S_B = (L_B - d_B) \pi d_B + \pi d_B^2 \quad (11)$$

Derivative of equation (9) writes:

$$\frac{dn_{EA}^G}{dt} = \frac{1}{R \cdot T} \left(V_B \cdot \frac{dP_t}{dt} + P_t \cdot \frac{\pi d_B^2}{4} \cdot \frac{dL_B}{dt} \right) \quad (12)$$

For the considered unit cell, the axial position in the channel and travelling time can then be related as:

$$U_{TP} \cdot dt = dz \quad (13)$$

Note that, as bubble volume varies along the channel, so does U_{TP} . Combining equations (8), (12) and (13) gives:

$$\frac{dL_B}{dz} = \left(\frac{k_G \cdot S_B}{U_{TP}} (P_{EA}^{vap} - P_{EA}) - V_B \cdot \frac{dP_t}{dz} \right) / \left(P_t \cdot \frac{\pi d_B^2}{4} \right) \quad (14)$$

Equation (14) applies to the local considered unit cell, *i.e.* to a specific axial position z . In the following steps, the k_G coefficient is considered invariant along the flow. So, in this equation, all parameters vary along z , except for d_B and k_G . It is recalled that the objective is to access to the time evolution of L_B , to compare it to measured values, and thus to identify k_G . To do so, calculation of d_B , V_B , S_B , $L_{B,0}$, P_t (and its derivative), U_{TP} , and P_{EA} , is needed. Their expressions will be derived later.

Variation of total pressure along the channel:

Total pressure includes hydrostatic pressure and shear stress between fluids as well as friction against the channel wall:

$$\frac{dP_t}{dz} = \frac{dP_{hydrostatic}}{dz} + \frac{dP_{friction}}{dz} \quad (15)$$

Neglecting the gas phase contribution to the hydrostatic pressure, it comes:

$$\frac{dP_{hydrostatic}}{dz} = -(1 - \varepsilon_G) \cdot \rho_L \cdot g \quad (16)$$

where ε_G is the local gas holdup within the flow.

The derivative expressed in equation (16) is negative for ascending flows.

To evaluate pressure loss due to friction in Taylor flow, the model derived by Warnier and colleagues was chosen [31], as it applies to a millimetric circular channel under similar hydrodynamic conditions to those of the present work. This model is valid for $Ca < 0.01$, $Re_B < 150$ and negligible velocity of the liquid in the film surrounding the gas bubbles. Accounting for the fraction of channel length occupied by the slugs, it gives:

$$\frac{dP_{friction}}{dz} = -f_s \cdot \frac{4}{d_c} \left(\frac{1}{2} \rho_L \cdot U_{TP}^2 \right) \left(\frac{L_S}{L_B + L_S} \right) \quad (17)$$

where f_s is the modified Fanning friction factor, taking into account the presence of the gas bubble in the unit cell:

$$f_s = \frac{16}{Re_{TP}} \cdot \left(1 + \frac{7.16 \times 3^{2/3}}{32} \cdot d_c \cdot \frac{f_B}{U_{LS}} \cdot \left(\frac{1}{Ca^{1/3} + 3.34 \cdot Ca} \right) \right) \quad (18)$$

with Re_{TP} the two-phase Reynolds number $\left(Re_{TP} = \frac{\rho_L \cdot U_{TP} \cdot d_c}{\mu_L} \right)$, f_B the bubble frequency defined as:

$$f_B = \frac{Q_G}{V_B} \quad (19)$$

Q_G and V_B are the local values of the volumetric gas flow rate and the bubble volume, respectively (V_B being given by equation (10)).

In addition, in the present work, pressure measurements at channel inlet and outlet for Taylor flows lead to adjust the model through a multiplying factor f_{corr} . Then it comes:

$$\frac{dP_{friction}}{dz} = -f_{corr} \cdot f_s \cdot \frac{4}{d_c} \left(\frac{1}{2} \rho_L \cdot U_{TP}^2 \right) \left(\frac{L_S}{L_B + L_S} \right) = -f_{corr} \cdot f_s \frac{4}{d_c} \left(\frac{1}{2} \rho_L \cdot U_{TP}^2 \right) \frac{U_{LS}}{U_{TP}} \quad (20)$$

where U_{LS} is the superficial velocity of liquid phase.

Note that the factor f_{corr} is identified for each performed experiment.

Finally, when combining equations (15), (16) and (20), the variation in total pressure along the tube writes:

$$\frac{dP_t}{dz} = -(1 - \varepsilon_G) \cdot \rho_L \cdot g - f_{corr} \cdot f_s \cdot \frac{4}{d_c} \left(\frac{1}{2} \rho_L \cdot U_{TP} \cdot U_{LS} \right) \quad (21)$$

This expression requires in addition the calculation of the gas phase hold-up ε_G .

Gas volume fraction in the unit cell ε_G :

The different velocities of the system are linked all together and lead to the determination of gas volume fraction:

$$U_{GS} = \beta_G \cdot U_{TP} = \varepsilon_G \cdot U_B \quad (22)$$

where β_G represents the ratio between volumetric gas flow rate and total fluid flow rate.

Constant bubble diameter d_B :

Lubrication films are too thin to be measured as the camera had to record a large ROI to catch several neighbouring bubbles (see section 2.3). To obtain their value, the two-phase velocity at bubble entrance $U_{TP,0}$ is first calculated on the basis on fluids flow rates. Bubble velocity at channel entrance, $U_{B,0}$, is then calculated thanks to the Bretherton model [32] by solving the following implicit equation:

$$\frac{U_{B,0} - U_{TP,0}}{U_{B,0}} = 1.29 \times (3 \cdot Ca_0)^{2/3} \quad (23)$$

Then, lubrication film thickness δ_f can be obtained via the relation developed by Aussilous and Quéré [33]:

$$\frac{\delta_f}{d_c} = \frac{0.66 \cdot Ca_0^{2/3}}{1 + 3.33 \cdot Ca_0^{2/3}} \quad (24)$$

Bubble diameter is deduced from:

$$d_B = d_c - 2\delta_f \quad (25)$$

Knowing d_B , bubble volume and bubble surface can be calculated thanks to equations (10) and (11), using the current solved value of L_B .

Boundary value $L_{B,0}$:

$L_{B,0}$ is deduced from the bubble volume at channel inlet $V_{B,0}$ through equation (10).

At any axial position in the channel, the various volumes can be expressed as:

$$V_{UC} = \frac{V_L}{1 - \varepsilon_G} \quad (26)$$

$$V_B = \varepsilon_G V_{UC} \quad (27)$$

It comes:

$$V_B = \frac{\varepsilon_G}{1 - \varepsilon_G} V_L \quad (28)$$

Liquid volume is unknown, but remains unchanged all along the channel. Based on this statement and on equation (28), bubble volume at any axial position in the channel – for example $V_{B,0}$ which is unknown – can be deduced from gas features measured at a reference axial position:

$$V_{B,0} = \frac{\varepsilon_{G,0}}{1 - \varepsilon_{G,0}} \cdot \frac{1 - \varepsilon_G}{\varepsilon_G} \cdot V_B \quad (29)$$

where the gas phase hold-up at the channel entrance, $\varepsilon_{G,0}$, is estimated from equation (22) using $U_{B,0}$ given by equation (23).

The chosen reference position corresponds to the end of the zone which is surrounded by the double jacket. Indeed, this is the farthest position from channel entrance, and the equilibrium between gas and liquid phases is assumed to be reached at that point. This reference axial position is called z^* . There, the different variables are defined: $V_B = V_B^*$, $L_B = L_B^*$, $\varepsilon_G = \varepsilon_G^*$ et $P_{EA} = P_{EA}^{vap}$. These

equilibrium parameters are obtained from processing the images recorded in the farthest IA from channel entrance, within the farthest ROI.

Two-phase velocity U_{TP} :

The liquid flow rate is assumed to be constant along the channel. On the contrary, the gas flow rate increases because of EA vaporization. As a consequence, so does U_{TP} . The superficial gas velocity is related to the total gas molar flow rate F_t^G and to the channel cross section A_c :

$$U_{GS} = \frac{F_t^G \cdot R \cdot T}{P_t \cdot A_c} \quad (30)$$

where:

$$F_t^G = \frac{P_t}{P_t - P_{EA}} \cdot F_{N_2,0}^G \quad (31)$$

(the molar nitrogen flow rate $F_{N_2}^G$ remaining unchanged).

Partial EA pressure P_{EA} and corrective factor f_{corr} for friction pressure evaluation:

Thus, the total volumetric gas flow rates at any location z can be linked to its value at channel entrance:

$$P_t \cdot Q_G = \frac{1}{1 - y_{EA}} \cdot P_{t,0} \cdot Q_{G,0} \quad (32)$$

where y_{EA} is the current molar fraction in EA as corresponding to the EA gas concentration C_{EA}^G .

In an analogous way, at the UC scale:

$$y_{AE} = 1 - \frac{P_{t,0} \cdot V_{B,0}}{P_t \cdot V_B} \quad (33)$$

Equation (33) is used to relate EA molar fractions at current position z and at the reference position:

$$y_{EA} = 1 - (1 - y_{EA}^*) \cdot \frac{P_t^* \cdot V_B^*}{P_t \cdot V_B} \quad (34)$$

Expressing y_{EA} with use of P_{EA} and P_t gives:

$$P_{EA} = P_t - (P_t^* - P_{EA}^{vap}) \cdot \frac{V_B^*}{V_B} \quad (35)$$

To complete this equation, the equilibrium total pressure P_t^* is needed. It is reached by integration of equation (21) from channel entrance to the current z position. To obtain an algebraic explicite expression for P_t^* , it is considered here that ε_G and U_{TP} (whose values are taken at z^* and z_{out} , respectively) are almost constant along the channel. This assumption sounds relevant since these variables reach their reference values soon after channel entrance. It comes:

$$P_t^* = P_{t,0} - (1 - \varepsilon_G^*) \rho_L \cdot g \cdot z^* - f_{corr} \cdot f_s \cdot \frac{4}{d_c} \left(\frac{1}{2} \rho_L \cdot U_{TP,out} \cdot U_L \right) z^* \quad (36)$$

So, to reach the value of P_{EA} at the current position z in the channel through equation (35), one still needs to evaluate ε_G^* and f_{corr} . These values will result from simultaneous solving of two non-linear algebraic equations:

- The first equation describes nitrogen molar conservation in the bubble from channel entrance to the equilibrium position; in this goal, equation (35) is used for $z = 0$ ($P_{EA} = 0$) and combined with the expression of bubble volume ratio (equation (29)):

$$P_{t,0}(1 - \varepsilon_G^*) \frac{\varepsilon_{G,0}}{(1 - \varepsilon_{G,0})} - (P_t^* - P_{EA}^{vap}) \varepsilon_G^* = 0 \quad (37)$$

- The second one results from integration of pressure gradient (equation (21)) from channel inlet to channel outlet (it is recalled that equation (21) holds the unknown parameter f_{corr}):

$$P_{t,0} - P_{t,out} - (1 - \varepsilon_G^*) \cdot \rho_L \cdot g \cdot z_{out} - f_{corr} \cdot f_s \cdot \frac{4}{d_c} \left(\frac{1}{2} \rho_L \cdot U_{TP,out} \cdot U_L \right) z_{out} = 0 \quad (38)$$

This equation shows the total pressures at both ends of the channel, $P_{t,0}$ and $P_{t,out}$: $P_{t,0}$ is measured, and $P_{t,out}$ is considered equal to the atmospheric pressure.

3.1.2 Model solving strategy

The variables d_B , V_B , S_B , ε_G , U_{TP} , P_{AE} and f_{corr} are now expressed as functions of the two unknown parameters L_B and P_t . Variables P_t^* , ε_G^* and f_{corr} are computed first (from algebraic equations (36) to (38)) from a specific routine. The final system to be solved consists in two non-linear differential equations (equations (14) and (21)) in which the two unknowns L_B and P_t appear. The coefficient k_G is a parameter to be tuned so that the calculated values of L_B match the experimental ones.

The boundary conditions to be used are:

$$P_t(z = 0) = P_{t,0} \quad (39)$$

$$L_B(z = 0) = L_{B,0} \quad (40)$$

$L_{B,0}$ is the guessed bubble size at channel entrance, as estimated from bubble volume values at different axial positions in the channel.

The entire system of equations is solved using MATLAB® (R2019a).

3.2 CFD approach for gas-side mass transfer assessment and analysis

3.2.1 Modeling framework and settings

The EA mass transfer is very fast, which compromises the accuracy of experimental k_G measurements. As mentioned in the introduction, numerical simulations allow assessing the measured values – or at least their order of magnitude –, as well as investigating the impact of experimental parameters such as temperature, flow velocity and solute diffusivity outside of the operating envelope of the present experimental tool.

These simulations involve the description of phenomena at the bubble scale, through the continuity and momentum equations (for each phase), and the transport equation for EA species in the gas phase. These equations and their relevant respective boundary conditions, as well as the selected CFD

software (COMSOL Multiphysics®), are reported in details in recent works [34, 35], which deal with the transfer of a pure gaseous species towards a liquid and thus numerically describe the liquid phase only. In these works, as well as in prior studies [36, 37], the unit cell (UC) approach is applied to describe Taylor flow in a cylindrical vertical milli-channel. It consists in modelling the phenomena for a single UC in a reference frame moving with the bubble. In this frame, the numerical problem is thus unsteady, and specific phenomena linked to disturbance at channel inlet and outlet are not described. To account for UC upward motion, the channel wall is considered to move at the velocity $-U_B$.

Inside the UC, the bubble is surrounded by two liquid slug halves. In the present work, the thermodynamic equilibrium is set for EA as boundary condition at the interface (concentration: $C_{EA}^{G,*}$), to compute EA concentration inside the bubble. As EA vapor is transferred to the gas phase, bubble volume increases, and force balance at the interface induces bubble surface distortion. This is computed thanks to the moving mesh approach, based on the Arbitrary Lagrangian–Eulerian (ALE) method, which is directly available in COMSOL Multiphysics®. Despite EA vaporization, temperature is assumed uniform in the UC: in other words, vaporisation heat is supposed efficiently carried away through the double jacket.

As the bubble expands in the UC while slug volume is constant, its velocity U_B increases. The wall velocity has thus to be adjusted all along bubble rise, in order to keep bubble position stable at UC center. This is performed by a numerical PID controller, specifically developed and linked to the computation.

Another specific difficulty in this work lays in the boundary conditions to be set at entrance and outlet faces of the modelled UC. In COMSOL Multiphysics® periodic conditions can be set, meaning that identical velocity profiles are specified for these two faces, and that a value is imposed as pressure drop (ΔP_t) over the UC. However, this value is unknown *a priori*, and crucial for gas phase description. A different approach is then adopted, where the UC is considered “open” (no periodic conditions but inlet and outlet boundary conditions). Authors who adopt this strategy [34, 38] recommend insuring the Poiseuille velocity profile at UC inlet face, together with a condition of fixed total pressure at outlet face. Pressure drop across the UC volume is then computed, as well as the velocity profile at outlet face. The velocity profiles at UC boundaries ought to be very similar: this point has to be checked.

3.2.2 Modeling strategy

As bubble expands within the UC, the liquid flow structure is impacted as well as EA mass transfer. Therefore, the momentum equations and the transport equation for EA are coupled and thus simultaneously solved. The problem is of course unsteady.

Note that COMSOL Multiphysics® does not take into account the mass source due to bubble growth (*i.e.* induced by interface motion: $C_{EA}^{G,*} \frac{dV_B}{dt}$). This contribution has to be added.

The increase of UC length is equal to that of bubble length, according to:

$$\frac{dL_{UC}}{dt} = \frac{1}{\pi r_c^2} \cdot \frac{dV_B}{dt} \quad (41)$$

So, a UC inlet and outlet boundaries are set to move, their velocity being equal to $\pm \frac{1}{2} \cdot \frac{dL_{UC}}{dt}$.

The mass transfer coefficient k_G is then calculated as follows:

$$k_G = \left(\frac{\Phi_{EA}^G}{C_{EA}^{G,*} - C_{EA,av}^G} \right) \cdot \frac{1}{S_B} \quad (42)$$

where Φ_{EA}^G is the diffusive mass transfer rate (in $\text{mol}\cdot\text{s}^{-1}$) of transferred EA at bubble interface, which is computed through concentration gradient integration along bubble surface, and $C_{EA,av}^G$ is the average EA concentration in the bubble.

3.2.3 Domain meshing

The UC domain to be meshed is divided into four regions: the two slug halves at UC ends, the bubble itself and the liquid zone close to the gas-liquid interface comprising the lubrication film between the bubble and the channel wall. A free mesh – composed of triangular cells – is built for these areas (Figure 3) and is refined in the vicinity of boundaries. On both sides of bubble surface and at channel wall, concentration and velocity (respectively) gradients may be sharp. So, a specific “boundary layer” mesh type is used there: composed of thin quadrangles, these mesh layers offer several cells normal to the boundary, thus allowing accurate gradient calculation.

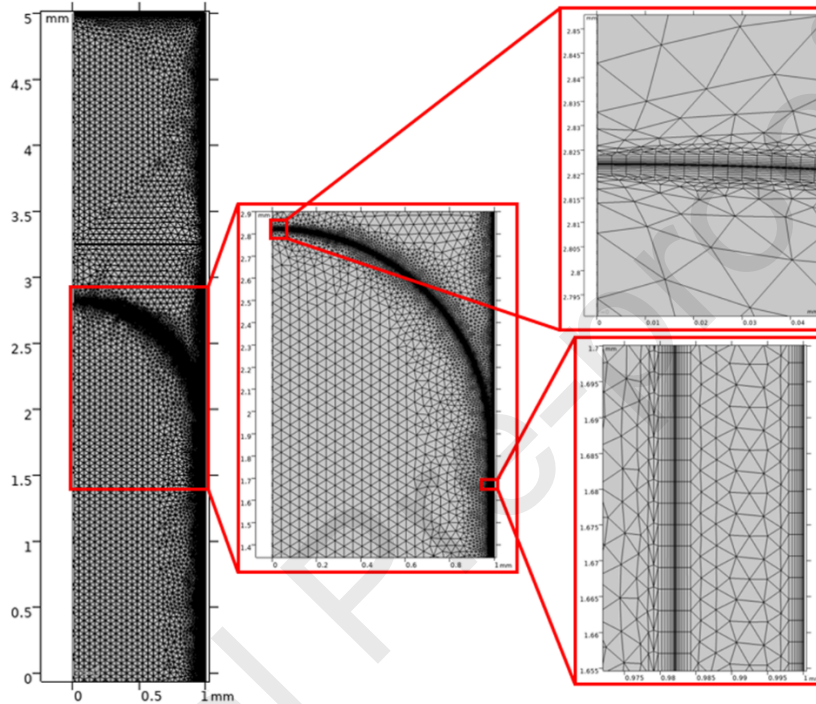


Figure 3. Mesh of the computed domain, zoomed into the areas close to the interface, and into the bubble nose and the lubrication film.

A specific study has been performed to check for the results sensitivity to the mesh and cell size, varying the number of cells in the boundary layers (from 6 to 12) and the maximum cell size near the interface and at the inlet/outlet domain boundaries. The coarsest mesh contained $\sim 60,000$ cells and the most refined one $\sim 190,000$ cells. Finally, depending on the considered geometry (*i.e.* on bubble and slug sizes), the used mesh contains $\sim 160,000$ cells, with $\sim 60,000$ quadrangles. The boundary layers offer 8 cells in the normal direction from interface or wall. For this selected mesh, the average quality values (ranging from 0 to 1) are 0.78 and 0.75 for the skewness and growth rate respectively (the value of 1 corresponds to the highest mesh quality for the considered metric).

4 Results and discussion

4.1 Experimental results for coefficient k_G

As example, case n°3 (see Table 2) is analysed here after in detail. For this experiment, performed at 324 K, a comparison is made on Figure 4a between the measured bubble lengths L_B (red marks) and the 1D-model predictions (solid lines). On this figure, the various ROIs are easily recognised as distinct groups of red marks, where each mark corresponds to an individual interrogated area (IA). For all the ROIs, the slope is similar, showing slow bubble expansion. A good agreement is found between experiment and model for any k_G value from $4 \cdot 10^{-3} \text{ m} \cdot \text{s}^{-1}$.

The 1D-model allows evaluating bubble volume variation at short times, *i.e.* before bubbles reach the first ROI: whatever the value of k_G , a fast expansion, due to EA transfer, is observed, related to the large local difference in EA partial pressure ($P_{EA}^{vap} - P_{EA}$). Further on, all computed curves meet the same constant moderate slope. At this stage, the curves predict the experimental values - except for one ROI where the measured values for L_B on the images are higher (+2%) than the overall trend, due to a possible local optical distortion. This slope actually corresponds to the pressure drop along the channel. Indeed, it is deduced from Figure 4b that, when this slope occurs, the equilibrium in EA is reached for the liquid and gas phases: the bubble length profiles along the channel thus converge to the same trend line for the different k_G values.

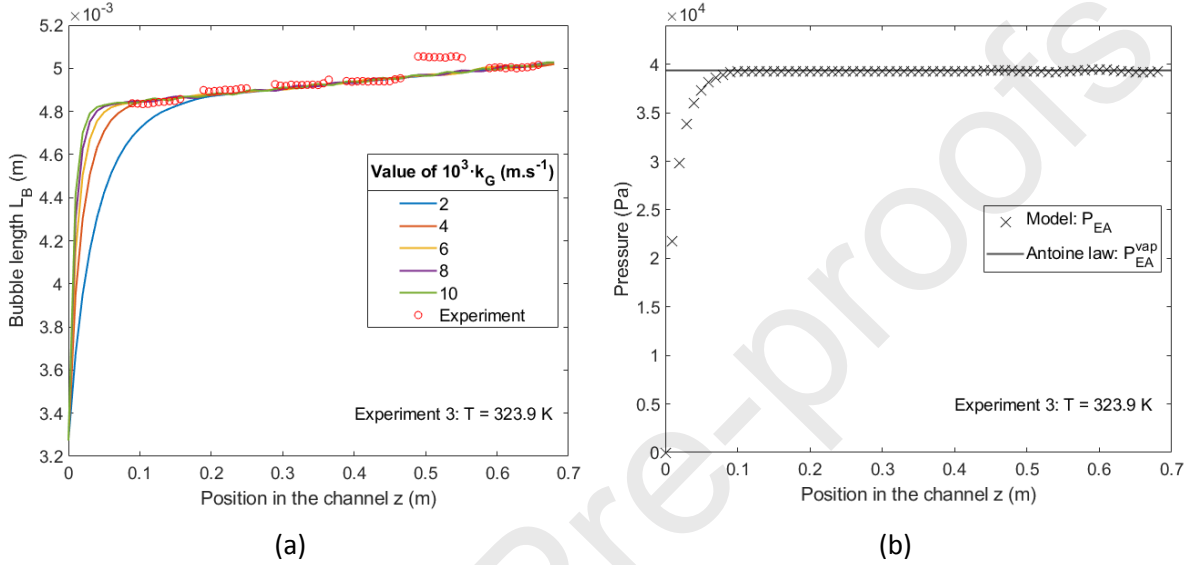


Figure 4. (a) Plot of bubble length along the channel: experimental values (red marks) and 1D-model predictions for various k_G values (solid lines); (b) plot of EA partial pressure along the channel according to the 1D-model for $k_G = 4 \cdot 10^{-3} \text{ m.s}^{-1}$. Experimental case n°3 (323.9 K).

So, the 1D-model clearly points out that the EA transfer is very fast and that it is almost completed before the flow enters the lowest ROI. As a consequence, bubble lengths extracted from images in this first ROI can only lead to a lower bound value of k_G .

As above mentioned, a corrective factor f_{corr} is used in equation (21) to adapt the friction pressure model [30] so that the calculated values of total pressure match the ones measured at channel inlet and outlet. For experimental case n°3, it is found $f_{corr} = 3.26$. As expected from equation (38), f_{corr} strongly depends on the total pressure measured at channel inlet, as shown in Table 3 for experiment n°3. Indeed, as the friction pressure represents a moderate part of the total pressure (less than 20%), a small difference in $P_{t,0}$ has a strong impact on f_{corr} values. The pressure transducer is set 0.4 m upstream from the channel inlet. Therefore, in the model, the value of f_{corr} compensates for the uncertainty in the inlet pressure, which is known within ± 0.01 bar. However, it should be noted that this uncertainty does not have a significant impact on the L_B profile predicted by the model for a given k_G value (Figure 5).

$P_{t,0}$ (bar)	f_{corr} (-)
1.05	0.87
1.06 (measured value)	3.26
1.07	5.69

Table 3. Sensitivity analysis for f_{corr} to the uncertainty on the inlet total pressure. Experimental case n°3 (323.9 K).

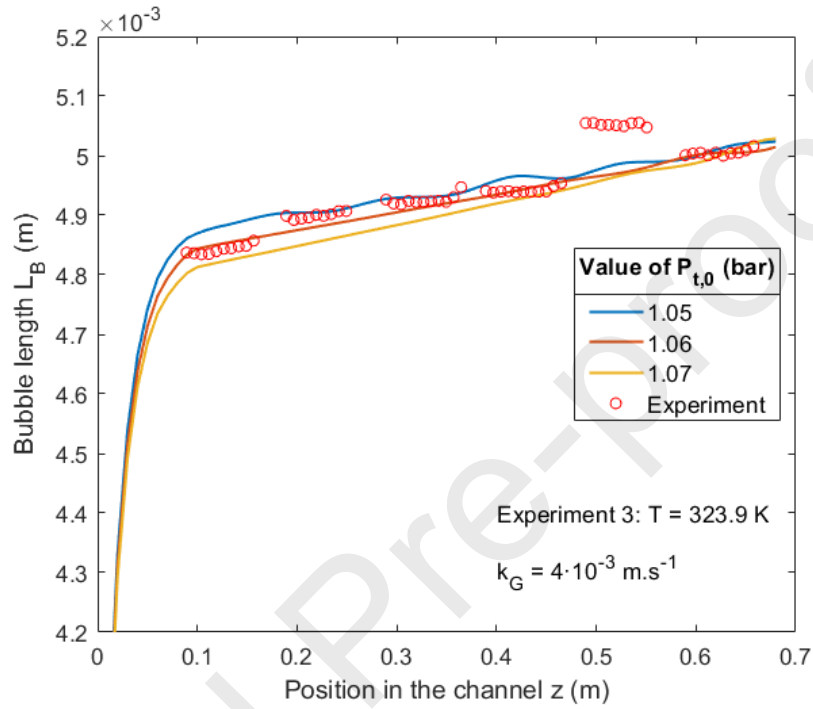


Figure 5. Impact of the pressure uncertainty on the L_B profile predicted by the model. $k_G = 4 \cdot 10^{-3} \text{ m.s}^{-1}$.

For each of the performed experiments, the lower bound value of k_G value is identified, which allows the 1D-model to match the respective experimental data. For instance, as for case n°3, L_B values are shown in Figure 6 for cases n° 4 and 6, together with the computed values from the 1D-model, with k_G values in the range $2 \cdot 10^{-3}$ to $1 \cdot 10^{-2} \text{ m.s}^{-1}$. From these two similar experiments (same fluids and $0.090 < U_{TP} < 0.14 \text{ m.s}^{-1}$), any value above $4 \cdot 10^{-3} \text{ m.s}^{-1}$ is in fact convenient for all experiments.

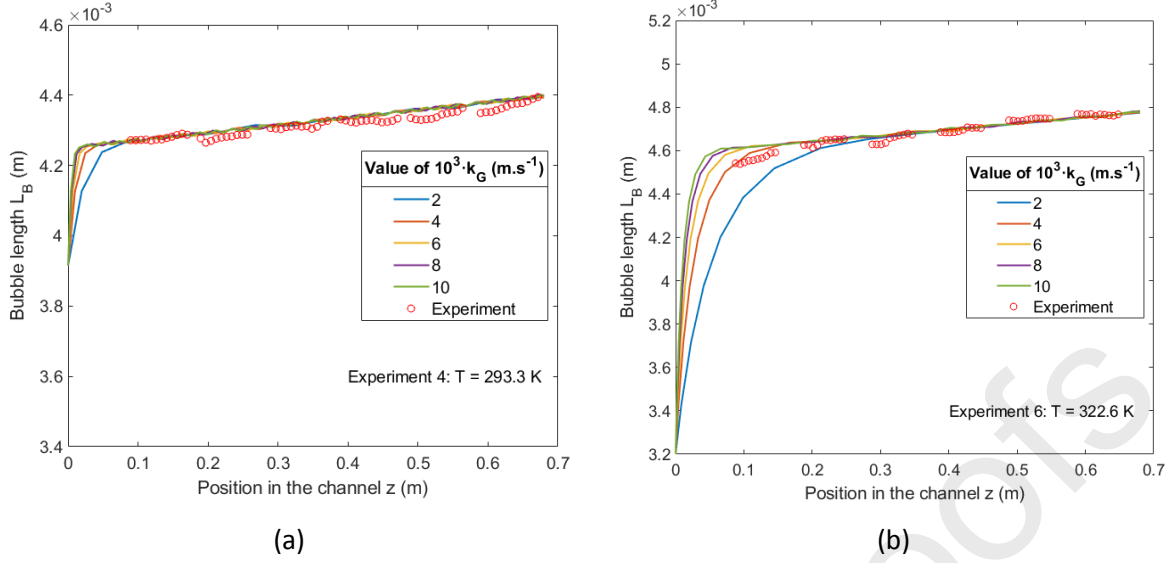


Figure 6. Variation of bubble length along the channel according to experimental values (red marks) and 1D-model predictions (continuous lines): (a) experimental case n°4 ($T = 293.3$ K); (b) experimental case n°6 ($T = 322.6$ K), $2 < k_G < 10 \cdot 10^{-3} \text{ m.s}^{-1}$ in the 1D-model.

4.2 Analysis of gas-side mass transfer by means of direct simulation

Thanks to direct simulations of EA vaporization in an isothermal UC travelling in a channel, wider ranges of operating conditions are investigated without any of the experimental bias as flow instability or temperature gradients. As mentioned, these simulations do not describe the injection of the two fluids, leading to mass transfer coefficients k_G related to developed Taylor flows. In the following, the impacts of the two-phase velocity, the flow rates ratio, the flow temperature and the diffusivity in gas phase of the transferred species are studied. The results – in terms of k_G – are also compared to mass transfer in a spherical bubble freely rising in a stagnant liquid.

4.2.1. Reference layout

Here after, the numerical simulation of experimental case n°4 is described (see Table 2), in which temperature is 293 K (leading to the lowest bubble expansion thus allowing for possible model simplification), the inlet flow rates are $Q_{N_2}^G = 0.5 \text{ NL.h}^{-1}$ and $Q_{EA}^L = 0.5 \text{ L.h}^{-1}$, corresponding to $U_{TP} = 0.088 \text{ m.s}^{-1}$ and to $\beta_G = 0.5$ (where $\beta_G = \frac{Q_{N_2}^G}{Q_{N_2}^G + Q_{EA}^L}$). The UC length is set at 10 mm, as measured on the recorded images at the inlet of the lowest ROI.

The computation involves the transient solving of the Navier-Stokes equations as well as EA transfer from the liquid phase into the bubble. A profile corresponding to Poiseuille law is set on the inlet face, the average velocity being U_{TP} . At the beginning of the calculation, the bubble is given the “ideal” shape and contains no EA , except for the interface concentration which is set at $C_{EA}^{G,*}$. Then, the bubble grows because of EA vaporization while travelling along the channel. It finally reaches a stable size corresponding to the thermodynamic equilibrium in EA . This final size is defined from equation (35) by:

$$\frac{V_{B,max}}{V_{B,0}} = \frac{1}{(1 - P_{EA}^{vap}/P_t)} \quad (43)$$

At 293 K and for atmospheric pressure, the volume increase (experiment n°4) is found to be 11%. The numerical simulation is in perfect agreement with this estimated expansion. The main features of the simulation results will be presented here after to assess the reliability of the computations.

4.2.2 Hydrodynamics analysis

The two-phase simulation performed with the ALE moving mesh module describes accurately the phases interactions, and the bubble distortion by viscous and capillary forces. The velocity field stabilizes rapidly (less than 1 s of physical time).

Bubble shape and lubrication film

The Capillary number is low ($Ca = 1.67 \cdot 10^{-3}$), leading to a negligible bubble distortion: its nose is slightly elongated, its rear barely flattened and shows a discreet bump (Figure 7).

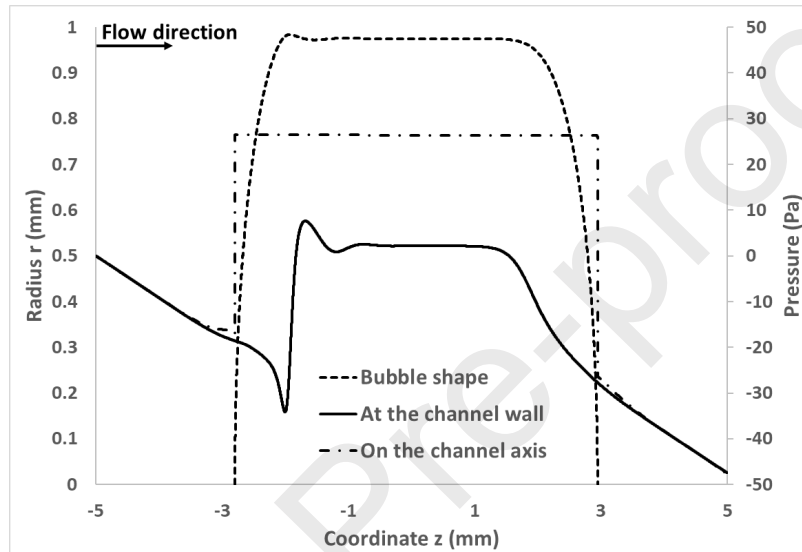


Figure 7. Bubble shape (dashed line), and pressure profile along the UC: pressure on channel axis (dash-dotted line) and at the channel wall (solid line). Simulation of reference case (experimental case n°4).

This shape agrees with the recorded images of bubbles in experimental case n°4 (Figure 8a). It is interesting to mention that Triplett et al. [39] obtained a similar shape for the air-water system and for an even larger capillary number ($5 \cdot 10^{-3}$), in a circular channel of 1.1 mm of inner diameter (Figure 8b). Note that, for U_{TP} twice larger and for temperature at 323 K, the bumps at bubble rear are more pronounced.

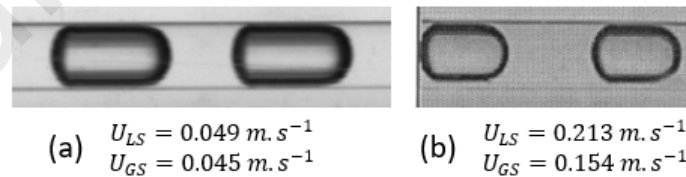


Figure 8. Images of bubbles whose shape is similar to the one predicted: (a) N_2 -ethyl acetate system, $d_c = 2$ mm, $Re_{TP} = 770$ and $Ca = 1.67 \cdot 10^{-3}$; (b) Triplett et al. [39], air-water system, $d_c = 1.1$ mm, $Re_{TP} = 400$ and $Ca = 5 \cdot 10^{-3}$ (values for Re_{TP} are given for illustration (and not Re_B values) since U_B is not provided in Triplett et al.'s work).

Therefore, the lubrication film thickness varies along the bubble from 16 μm (at bubble rear) to 25 μm (bubble center), whereas the estimated thickness of 18 μm for an “ideal” shape bubble (used as initial thickness).

Pressure profile

Far from the bubble in the UC, the pressure drop (induced by friction effect and static pressure variation) occurs at constant rate (Figure 7), as expected for flows close to the Hagen-Poiseuille reference. Near bubble rear, interface distortion generates pressure oscillations, while pressure drops drastically at bubble nose. In the area of constant thickness lubrication film, shear stress is negligible and pressure is stable.

Thus, pressure variation along UC axis is significant along the liquid slugs only. For the simulated case, pressure drop across the UC is 47.4 Pa.

Velocity profiles and streamlines

The simulation is run without periodicity condition for inlet and outlet faces. Thus, the outlet velocity profile is checked and found to be identical to the inlet one (Poiseuille profile, with less than 2% difference), assessing the periodicity of the flow for the UC borders, even for this short UC. The lubrication film is observed to be quasi-stagnant. However, a short area of liquid acceleration exists at bubble rear where the film slightly slims.

Streamlines are shown in Figure 9. Circulation loops appear inside the liquid slugs, as well as inside the bubble, near its nose and rear and in the vicinity of the lubrication film. This has often been observed for simulated Taylor flows (see for instance [34]).

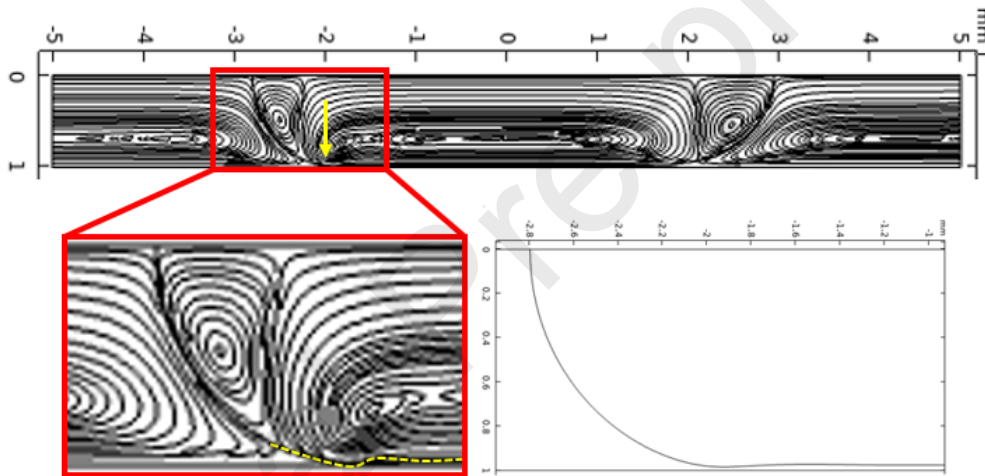


Figure 9. Streamlines in the bubble and in the liquid slugs. Zoomed view for bubble rear (as slightly distorted). Reference case (experimental case n°4).

4.2.3 Transport phenomena inside the bubble

Mass transport of EA inside the bubble is simultaneously solved. The gas diffusivity of EA in nitrogen has been estimated to $8.8 \cdot 10^{-6} \text{ m}^2 \cdot \text{s}^{-1}$ from the Fuller et al.'s correlation [40].

Contour of EA concentration in the bubble and time variation of the average concentration

The field of EA concentration in the bubble at different instant times is shown in Figure 10a, while the UC travels along the channel. Gradients in EA concentration exist near the interface all around the bubble, and are confined within a quasi-constant thickness film. Slight disturbance of this layer is due to the gas circulation loops and to the interface distortion. Such a concentration distribution suggests a diffusion-controlled transport. Note that this has been observed in the numerical results from Colombet et al. [27], dealing with a bubble rising freely in a stagnant liquid. The limited contribution of convective effects for EA transport inside the bubble induces a limited impact of the two-phase velocity U_{TP} , as will be discussed later.

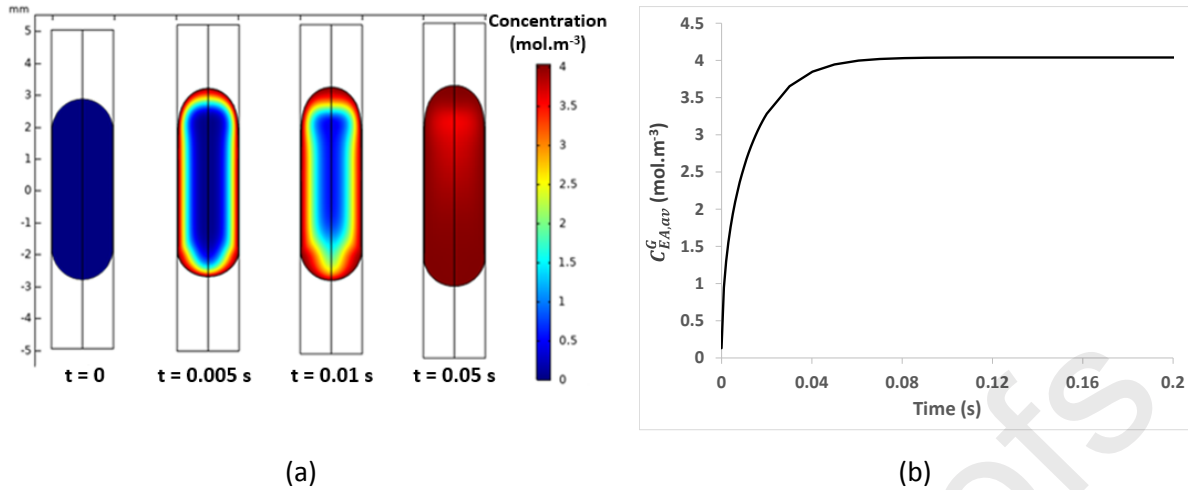


Figure 10. Mass transport inside the bubble: (a) successive EA concentration fields; (b) time-evolution of the average EA concentration. Reference case (experimental case $n^{\circ}4$).

The average EA concentration inside the bubble increases up to a plateau value (Figure 10b) when thermodynamic equilibrium is reached: 99.9% of $C_{EA}^{G,*}$ was obtained in 0.1 s for the reference case, which corresponds to a distance of ca. 1 cm travelled by the UC. This confirms that the equilibrium is rapidly reached, as observed in the experiments. What is more, the disturbances due to the phases entrance in the channel are not accounted for in these numerical computations, and the bubble is considered free of any EA at the initial step.

Mass transfer coefficient k_G

The time evolution of the k_G coefficient is presented in Figure 11. When the simulation starts, values as high as 0.1 m.s^{-1} are observed. Indeed, at the beginning, EA concentration at interface is very different from the average bubble concentration. Then k_G sharply decreases, reaches a minimum before stabilizing after 0.2 s. Again, such a behavior was reported in the work of Colombet et al. [27] for a free rising bubble with bubble Péclet numbers of 80 and 160. In the present work, $Pe \sim 20$.

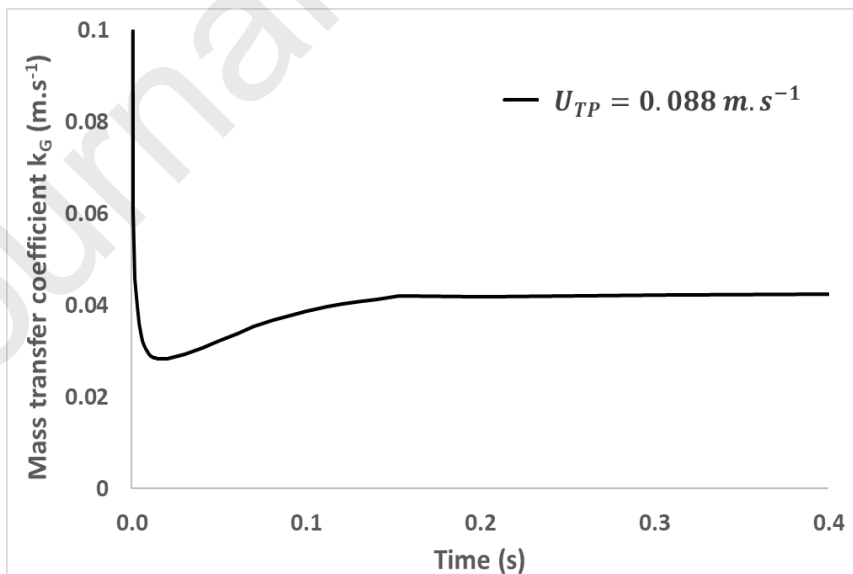


Figure 11. Time-evolution of the k_G coefficient along computational calculations. Reference case (experimental case $n^{\circ}4$).

4.2.4 Influence of operating conditions on k_G

The following parameters are successively varied:

- two-phase velocity U_{TP} ,
- ratio between volumetric gas and total flow rates β_G ,
- temperature T (two values are checked: 293 and 323 K).

Table 4 gathers the stabilized k_G values. Note that, for the study of the first two parameters, hydrodynamics was modelled first and mass transport of EA inside the bubble was computed afterwards by use of a fixed velocity field (thus neglecting bubble volume expansion), because these computations run much faster.

Results obtained at 293 K confirm that the method is then reliable: only 5% discrepancy ($4.22 \cdot 10^{-2}$ vs. $4.45 \cdot 10^{-2} \text{ m}\cdot\text{s}^{-1}$) was observed between the derived k_G value and the value from the simultaneous modelling of coupled phenomena.

Sensitivity analysis to U_{TP} : $D_{EA-N_2} = 8.8 \cdot 10^{-6} \text{ m}^2 \cdot \text{s}^{-1}$, $\beta_G = 0.5$, $T = 293 \text{ K}$			
$U_{TP} (\text{m}\cdot\text{s}^{-1})$	0.088	0.044	0.180
$k_G (\text{m}\cdot\text{s}^{-1})$	$4.22 \cdot 10^{-2}$	$2.95 \cdot 10^{-2}$	$5.89 \cdot 10^{-2}$
Sensitivity analysis to β_G : $D_{EA-N_2} = 8.8 \cdot 10^{-6} \text{ m}^2 \cdot \text{s}^{-1}$, $U_{TP} = 0.088 \text{ m}\cdot\text{s}^{-1}$, $T = 293 \text{ K}$			
β_G	0.5	0.3	0.7
$k_G (\text{m}\cdot\text{s}^{-1})$	$4.22 \cdot 10^{-2}$	$3.99 \cdot 10^{-2}$	$4.17 \cdot 10^{-2}$
Sensitivity analysis to T : $U_{TP} = 0.088 \text{ m}\cdot\text{s}^{-1}$, $\beta_G = 0.5$			
$T (\text{K})$	293	323	
$D_{EA-N_2} (\text{m}^2 \cdot \text{s}^{-1})$	$8.8 \cdot 10^{-6}$	$1.0 \cdot 10^{-5}$	
$k_G (\text{m}\cdot\text{s}^{-1})$	$4.45 \cdot 10^{-2}$	$5.17 \cdot 10^{-2}$	

Table 4. Effect of operating parameters onto the k_G value. Hydrodynamics and mass transport were computed sequentially for the sensitivity analysis to U_{TP} and β_G at 293 K, but simultaneously for T effect.

On the investigated range, when U_{TP} is doubled, k_G is increased by 40%. This suggests that the latter is linked to the square root of the two-phase velocity. Such a scaling relation is conventionally proposed by authors for k_L estimation, for non-reactive absorption systems [15, 20, 41]. Thus, convective effects contribute to gas-side mass transfer.

Flow rates ratio β_G , whose value is close to that of the gas volume fraction (ε_G), shows a minor impact on k_G , for a given two-phase velocity U_{TP} . So, even for long bubbles, the structure of concentration gradients in the vicinity of the interface (Figure 10a) is conserved.

The k_G value is obviously sensitive to temperature: from 293 K to 323 K (bubble expansion being accounted for), it increases by 16%. However, in this range, physico-chemical properties of the considered fluids do not significantly vary (see Table 1) and hydrodynamics are not modified. One key-phenomenon is the increase with temperature of EA diffusivity in nitrogen, which is calculated to be 10%, according to literature [40]. Bubble expansion contributes too: at 323 K, bubble volume expands by 59% whereas it expands by 11% at 293 K. So, bubble velocity is significantly higher at 323 K, leading to k_G increase, as mentioned earlier (without accounting for its effect, k_G would increase by 10% only).

As a conclusion from this numerical study, for the $N_2 - EA$ system and for $0.09 < U_{TP} < 0.18 \text{ m}\cdot\text{s}^{-1}$, the k_G coefficient varies in the range $2 \cdot 10^{-2}$ and $6 \cdot 10^{-2} \text{ m}\cdot\text{s}^{-1}$, depending on bubble velocity.

These calculations confirm the lower bound value of k_G that has been experimentally pointed out ($k_G > 4 \cdot 10^{-3} \text{ m}\cdot\text{s}^{-1}$) for the same order of magnitude of U_{TP} .

4.2.5 Extrapolation to other gas-liquid systems

To widen the discussion to other gaseous systems – in particular systems of industrial interest, as those involved for gas sweetening ($\text{CO}_2 - \text{CH}_4$) or CO_2 capture from flue gas ($\text{CO}_2 - \text{N}_2$) – gas diffusivity D_G is to be varied in the gas-side mass transfer computations. For instance, CO_2 diffusion coefficient in nitrogen is $1.67 \cdot 10^{-5} \text{ m}^2\cdot\text{s}^{-1}$ at 298 K following Ellis and Holsen [42], *i.e.* twice the EA diffusivity in nitrogen.

For this study again, hydrodynamics is modelled first and mass transport of EA inside the bubble is computed afterwards, based on the converged velocity field. Here, D_G is varied in a far larger range ($2 \cdot 10^{-7}$ to $5 \cdot 10^{-5} \text{ m}^2\cdot\text{s}^{-1}$), leading to values for Péclet number (Pe) from 3 to 1,000. This allows plotting the Sherwood number (Sh) versus Pe . It is interesting to compare these results to those which were numerically obtained for a free rising bubble in stagnant liquid [27], as transport phenomena inside the bubble and concentration layers at bubble surface have surprisingly been found similar for these two kinds of bubble (section 4.2.3).

The diffusivity value is found to drastically impact k_G : starting with a value of $5 \cdot 10^{-7} \text{ m}^2\cdot\text{s}^{-1}$, an increase of D_G by a factor 10 or 100 results in a k_G increase by a factor 6.6 or 30, respectively.

As mentioned in section 1.2.3, Colombet and co-workers [27] investigate the gas-side mass transfer for a free bubble, by varying Sherwood and Péclet numbers: $Sh = \frac{k_G \cdot d_B}{D_G}$, and $Pe = \frac{U_B \cdot d_B}{D_G}$. They report that the plot of the asymptotic Sherwood value Sh_∞ (obtained when $t \rightarrow \infty$) with respect to Pe exhibits two plateaus (Figure 12): when $Pe \rightarrow 0$, Sh_∞ reaches its minimal values (6.58), and, when $Pe \rightarrow \infty$, Sh_∞ extends to its maximal value (~ 18). Convective effects, when intensified in regard with diffusive ones, have thus a limited impact onto gas-side mass transport.

Interestingly, for confined Taylor bubbles, the sigmoidal shape of Sh plot versus Pe is also true (Figure 12), though the bounding values are found slightly different: for $Re_B = 387$, the minimum Sh_∞ value is 5.7 (corresponding to $k_G = 2.5 \cdot 10^{-2} \text{ m}\cdot\text{s}^{-1}$ for EA at 293 K in a 2 mm channel), the maximum one is ~ 20 . These discrepancies may be attributed to the difference in shapes of the two considered bubbles, or to the fact that, for Taylor bubbles, U_B is not equal to the relative velocity between the phases. However, the observed similarities confirm that convective effects are limited inside the Taylor bubbles too.

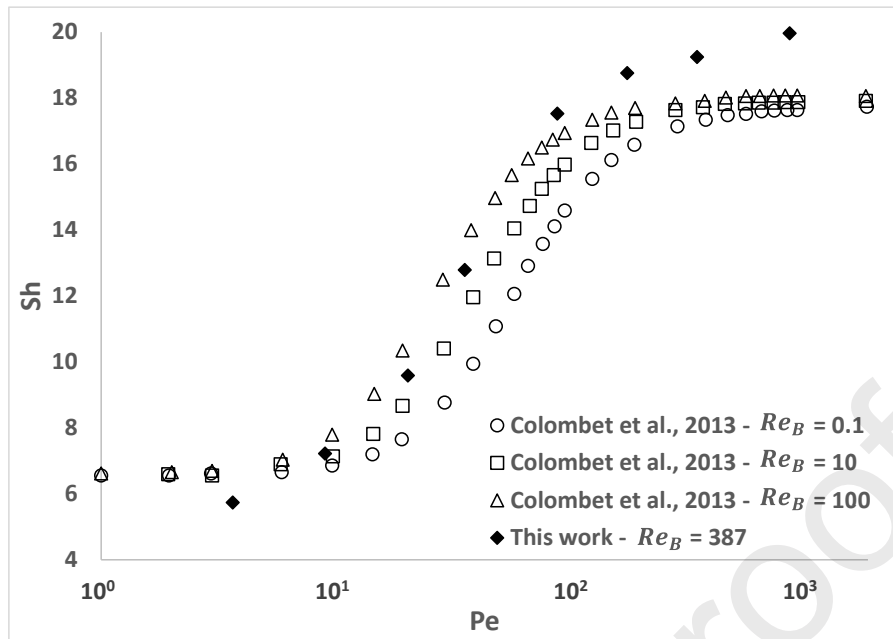


Figure 12. Evolution of Sh number versus Pe number, and comparison to the numerical results obtained by Colombet et al. [27] for a free bubble rising in a stagnant liquid.

4.3 Mass transfer resistances in Taylor flow for industrial applications

The mass transfer resistances on both sides of gas-liquid interface, $(H \cdot R \cdot T)/k_G$ and $\frac{1}{(E \cdot k_L)}$ can now be compared for a gas-liquid system of industrial interest. As an example, absorption of CO_2 from natural gas at 293 K by means of amine aqueous solutions is referred to. Natural gas is here modelled as a mixture of methane (95% vol.) and carbon dioxide (5% vol.), and an aqueous solution with 30 wt.% of N-methyldiethanolamine (*MDEA*) is selected.

On the one hand, the experimental lower bound value of k_G ($4 \cdot 10^{-3} \text{ m} \cdot \text{s}^{-1}$) obtained from experiments of *EA* vaporization in nitrogen is considered. This value may be corrected by the square roots of the considered gas diffusivities, as usually advised in the literature [23]; however the diffusivity of *EA* in nitrogen and that of CO_2 in CH_4 are very close ($\sim 8 \cdot 10^{-6} \text{ m}^2 \cdot \text{s}^{-1}$). According to [43], the Henry constant for CO_2 in *MDEA* at 293 K is $3 \cdot 10^{-4} \text{ mol} \cdot \text{m}^{-3} \cdot \text{Pa}^{-1}$. This leads to $(\frac{H \cdot R \cdot T}{k_G})_{max} < 185 \text{ s} \cdot \text{m}^{-1}$.

On the other hand, the minimum and maximum Sh_∞ numbers (5.7 and 20 respectively) obtained from the numerical study (section 4.2.5) are scaled with CO_2 diffusivity in CH_4 and with the channel diameter used in this work ($2 \cdot 10^{-3} \text{ m}$) to get another estimation for k_G : values of $2.3 \cdot 10^{-2} \text{ m} \cdot \text{s}^{-1}$ and $8.0 \cdot 10^{-2} \text{ m} \cdot \text{s}^{-1}$ (respectively) are obtained. This leads to $9 < \frac{H \cdot R \cdot T}{k_G} < 32 \text{ s} \cdot \text{m}^{-1}$.

Available correlations from the literature [12, 18, 44] allow estimating the liquid-side mass transfer coefficient k_L at 293 K in the range of gas and liquid flow rates ($U_{TP} \sim 0.1 \text{ m} \cdot \text{s}^{-1}$) considered in the present work. When needed in the correlation, the interfacial area or bubble size were assumed similar to those measured in this work. This led to $3.9 \cdot 10^{-5} < k_L < 3.4 \cdot 10^{-4} \text{ m} \cdot \text{s}^{-1}$. In this system (30 wt.% *MDEA* in water, 293 K, 1 atm), E is estimated between 1 and 2, using kinetics data from Rinker et al. [43]. It comes: $1.5 \cdot 10^3 < \frac{1}{E \cdot k_L} < 2.6 \cdot 10^4 \text{ s} \cdot \text{m}^{-1}$.

Therefore, in these operating conditions, the gas-side mass transfer resistance is always lower than 12% of the liquid-side one, as k_G is higher than $4 \cdot 10^{-3} \text{ m} \cdot \text{s}^{-1}$, according to the experimental results. However, as explained in previous sections, the *EA* vaporization is so fast that the measured k_G value is a lower bound value.

Thus, the gas-side mass transfer resistance in Taylor flows for a $N_2 - CO_2 - MDEA - H_2O$ system would be negligible (less than 2%) when the two-phase velocity is about $0.1 \text{ m} \cdot \text{s}^{-1}$.

5 Conclusions

Previous works on Taylor flow have not investigated the significance of the gas-side mass transfer coefficient k_G so far. In this work the authors selected and developed an experimental method, based on bubble expansion record, to estimate k_G value in a circular channel (1 m long, 2 mm inner diameter) fed with nitrogen gas and pure ethyl acetate (*EA*). *EA* transfer was found very fast. For practical constraints, images could not be recorded close enough to channel entrance. However, the recorded images proved that the order of magnitude of k_G is at least a few $\text{mm} \cdot \text{s}^{-1}$ when $U_{TP} \sim 0.1 \text{ m} \cdot \text{s}^{-1}$.

CFD simulations advantageously completed the experimental investigation and further estimated the order of magnitude: $k_G \sim 10^{-2} \text{ m} \cdot \text{s}^{-1}$ when $0.09 < U_{TP} < 0.18 \text{ m} \cdot \text{s}^{-1}$. The migration of *EA* vapour inside the bubble suggests a significant contribution of diffusion in regard with the convective effects. k_G is found to be sensitive to U_{TP} and to the temperature, but not to the gas volume fraction. Both the time-evolution of k_G and the relationship between the asymptotic Sherwood value Sh_∞ ($t \rightarrow \infty$) and bubble Péclet number are found similar to the observations from Colombet and co-workers [27] concerning a spherical bubble freely rising in quiescent liquid.

For the first time, to the authors' knowledge, these results allow assessing the gas-side mass transfer resistance for any gas-liquid system in Taylor flow. As an illustration, it was evidenced that, for a gas-liquid system of industrial interest (absorption of CO_2 in aqueous solution of *MDEA*), gas-side mass transfer resistance is lower than the liquid-side one by at least one order of magnitude, confirming the assumption of negligible gas-side resistance usually made in this field.

Acknowledgements

The authors thank the ANRT for financial support and the FERMaT federation for lending the high-speed camera. They are grateful to the technical team of *Laboratoire de Génie Chimique*, namely Bruno Boyer, Lahcen Farhi and Quentin Ribiere, and to Emmanuel Cid for his expertise in shadowgraphy measurements, to Dr. Pierre Albrand (LGC Toulouse) and COMSOL France for their help and advice on the CFD simulations and to Dr. Benjamin Lalanne (LGC Toulouse) for the constructive discussions on this topic.

Notations

Acronyms

ALE	Arbitrary Lagrangian–Eulerian
EA	Ethyl Acetate
IA	Interrogation Area
MEA	MonoEthanolAmine
MDEA	N-MethylDiEthanolAmine
ROI	Region Of Interrogation
UC	Unit Cell

Roman letters

A	Cross section, m^2
A, B, C	Constants for the Polák and Mertl [30] model; A and B dimensionless, C in K
a	Specific interfacial area, m^{-1}
C	Concentration, $mol.m^{-3}$
D	Diffusivity, $m^2.s^{-1}$
d	Diameter, m
E	Enhancement factor, (-)
F	Molar flow rate, $mol.s^{-1}$
f_{acq}	Acquisition frequency, s^{-1}
f_{corr}	Corrective factor for the Fanning factor in the model of Warnier et al. [31], (-)
f_s	Fanning factor in the Warnier model [31], (-)
g	Gravitational constant, $m.s^{-2}$
H	Henry constant, $mol.m^{-3}.Pa^{-1}$
K or k	Mass transfer coefficient, $m.s^{-1}$
L	Length, m

N	Molar flow rate per unit interfacial area, $\text{mol}\cdot\text{m}^{-2}\cdot\text{s}^{-1}$
n	Mole number, mol
P	Pressure, Pa
Q	Volumetric flow rate, $\text{m}^3\cdot\text{s}^{-1}$
R	Universal gas constant, $\text{J}\cdot\text{mol}^{-1}\cdot\text{K}^{-1}$
r	Radius, m
S	Surface, m^2
T	Temperature, K
t	Time, s
U	Velocity, $\text{m}\cdot\text{s}^{-1}$
V	Volume, m^3
y	Gas phase molar fraction, (-)
z	Coordinate, m

Dimensionless numbers

Ca	Capillary number, $Ca = \frac{\mu_L \cdot U_B}{\sigma_L}$
Pe	Péclet number, $Pe = \frac{U_B \cdot d_B}{D_G}$
Re	Reynolds number, $Re = \frac{\rho_L \cdot U \cdot d}{\mu_L}$
Sh	Sherwood number, $Sh = \frac{k_G \cdot d_B}{D_G}$
We	Weber number, $We = \frac{\rho_L \cdot U_B^2 \cdot d_c}{\sigma_L}$

Greek letters

β	Ratio between superficial gas velocity and two-Phase velocity, (-)
Δ	Related to a variation, (-)
δ	Thickness, (m)
ε	Volumetric fraction, (-)
μ	Dynamic viscosity, Pa.s
ρ	Density, $\text{kg}\cdot\text{m}^{-3}$
σ	Surface tension, $\text{N}\cdot\text{m}^{-1}$
Φ	Diffusive mass transfer rate, $\text{mol}\cdot\text{s}^{-1}$

Subscripts ou superscripts

A	Related to species A to be transferred
av	Related to average value
B	Related to the bubble
c	Related to the channel
EA	Related to Ethyl Acetate

<i>exp</i>	Related to experiment
<i>f</i>	Related to lubrication film
<i>G</i>	Related to the gas phase
<i>i</i>	Interface
<i>in or 0</i>	Defined at channel inlet
<i>L</i>	Related to the liquid phase
<i>max</i>	Related to maximum value
<i>N₂</i>	Related to nitrogen
<i>out</i>	Defined at channel outlet
<i>S</i>	Superficial (for velocities), or related to slug (for length)
<i>TP</i>	Related to the Two-Phase flow
<i>t</i>	Total (pressure)
<i>UC</i>	Related to Unit Cell
<i>vap</i>	Vapour equilibrium (for partial pressure)
*	Defined at liquid-vapour equilibrium

References

- [1] Thulasidas, T.C., Abraham, M.A., Cerro, R.L., 1999. Dispersion during bubble-train flow in capillaries. *Chem. Eng. Res. Des.* 54, 61–76. [https://doi.org/10.1016/S0009-2509\(98\)00240-1](https://doi.org/10.1016/S0009-2509(98)00240-1)
- [2] Kreutzer, M.T., Kapteijn, F., Moulijn, J.A., Heiszwolf, J.J., 2005. Multiphase monolith reactors: Chemical reaction engineering of segmented flow in microchannels. *Chem. Eng. Sc.* 60, 5895–5916. <https://doi.org/10.1016/j.ces.2005.03.022>
- [3] Cybulski, A., Moulijn, J.A., 2005. Structured catalysts and reactors. CRC press.
- [4] Angeli, P., Gavriilidis, A., 2008. Hydrodynamics of Taylor flow in small channels: A Review. *Proc. Inst. Mech. Eng. C. J. Mech. Eng. Sci.* 222, 737–751. <https://doi.org/10.1243/09544062JMES776>
- [5] Haase, S., Murzin, D.Yu., Salmi, T., 2016. Review on hydrodynamics and mass transfer in minichannel wall reactors with gas–liquid Taylor flow. *Chem. Eng. Res. Des.* 113, 304–329. <https://doi.org/10.1016/j.cherd.2016.06.017>
- [6] Delparish, A., Avci, A.K., 2016. Intensified catalytic reactors for Fischer-Tropsch synthesis and for reforming of renewable fuels to hydrogen and synthesis gas. *Fuel Process. Technol.* 151, 72–100. <https://doi.org/10.1016/j.fuproc.2016.05.021>
- [7] Haase, S., Bauer, T., Graf, E., 2020. Gas–liquid flow regime prediction in minichannels: A dimensionless, universally applicable approach. *Ind. Eng. Chem. Res.* 59, 3820–3838. <https://doi.org/10.1021/acs.iecr.9b03756>
- [8] Su, H., Wang, S., Niu, H., Pan, L., Wang, A., Hu, Y., 2010. Mass transfer characteristics of H₂S absorption from gaseous mixture into methyl-diethanolamine solution in a T-junction microchannel. *Sep. Purif. Technol.* 72, 326–334. <https://doi.org/10.1016/j.seppur.2010.02.024>

- [9] Kundu, A., Basu, J.K., Das, G., 2012. A novel gas–liquid contactor for chemisorption of CO₂. *Sep. Purif. Technol.* 94, 115–123. <https://doi.org/10.1016/j.seppur.2011.11.016>
- [10] Pan, M.-Y., Qian, Z., Shao, L., Arowo, M., Chen, J.-F., Wang, J.-X., 2014. Absorption of carbon dioxide into N-methyldiethanolamine in a high-throughput microchannel reactor. *Sep. Purif. Technol.* 125, 52–58. <https://doi.org/10.1016/j.seppur.2014.01.033>
- [11] Makarem, M.A., Farsi, M., Rahimpour, M.R., 2019. Applications of minichannels in gas absorption: A review. *Mod. Approaches Oceanogr. Petrochem. Sci.* 149, 207–216. <https://doi.org/10.32474/MAOPS.2019.02.000149>
- [12] Irandoust, S., Ertlé, S., Andersson, B., 1992. Gas-liquid mass transfer in Taylor flow through a capillary. *Can. J. Chem. Eng.* 70, 115–119. <https://doi.org/10.1002/cjce.5450700116>
- [13] Berčić, G., Pintar, A., 1997. The role of gas bubbles and liquid slug lengths on mass transport in the Taylor flow through capillaries. *Chem. Eng. Sc.* 52, 3709–3719. [https://doi.org/10.1016/S0009-2509\(97\)00217-0](https://doi.org/10.1016/S0009-2509(97)00217-0)
- [14] Sobieszuk, P., Pohorecki, R., Cygański, P., Grzelka, J., 2011. Determination of the interfacial area and mass transfer coefficients in the Taylor gas–liquid flow in a microchannel. *Chem. Eng. Sc.* 66, 6048–6056. <https://doi.org/10.1016/j.ces.2011.08.029>
- [15] van Baten, J.M., Krishna, R., 2004. CFD simulations of mass transfer from Taylor bubbles rising in circular capillaries. *Chem. Eng. Sc.* 59, 2535–2545. <https://doi.org/10.1016/j.ces.2004.03.010>
- [16] Ganapathy, H., Shooshtari, A., Dessiatoun, S., Alshehhi, M., Ohadi, M., 2014. Fluid flow and mass transfer characteristics of enhanced CO₂ capture in a minichannel reactor. *Appl. Energ.* 119, 43–56. <https://doi.org/10.1016/j.apenergy.2013.12.047>
- [17] Ganapathy, H., Shooshtari, A., Dessiatoun, S., Ohadi, M.M., Alshehhi, M., 2015. Hydrodynamics and mass transfer performance of a microreactor for enhanced gas separation processes. *Chem. Eng. J.* 266, 258–270. <https://doi.org/10.1016/j.cej.2014.12.028>
- [18] Butler, C., Lalanne, B., Sandmann, K., Cid, E., Billet, A.-M., 2018. Mass transfer in Taylor flow: Transfer rate modelling from measurements at the slug and film scale. *Int. J. Multiph. Flow* 105, 185–201. <https://doi.org/10.1016/j.ijmultiphaseflow.2018.04.005>
- [19] Durgadevi, A., Pushpavanam, S., 2018. An experimental and theoretical investigation of pure carbon dioxide absorption in aqueous sodium hydroxide in glass millichannels. *J. CO₂ Util.* 26, 133–142. <https://doi.org/10.1016/j.jcou.2018.05.002>
- [20] Yang, L., Dietrich, N., Loubière, K., Gourdon, C., Hébrard, G., 2016. Visualization and characterization of gas–liquid mass transfer around a Taylor bubble right after the formation stage in microreactors. *Chem. Eng. Sc.* 143, 364–368. <https://doi.org/10.1016/j.ces.2016.01.013>
- [21] Danckwerts, P.V., 1970. *Gas-liquid reactions*, McGraw-Hill chemical engineering series. McGraw-Hill Book Co., New-York.
- [22] Hegely, L., Roesler, J., Alix, P., Rouzineau, D., Meyer, M., 2017. Absorption methods for the determination of mass transfer parameters of packing internals: A literature review. *AIChE J.* 63, 3246–3275. <https://doi.org/10.1002/aic.15737>
- [23] Vidwans, A.D., Sharma, M.M., 1967. Gas-side mass transfer coefficient in packed columns. *Chem. Eng. Sc.* 22, 673–684. [https://doi.org/10.1016/0009-2509\(67\)80051-4](https://doi.org/10.1016/0009-2509(67)80051-4)

- [24] Roustan, M., 2004. Absorption en traitement d'air. Techniques de l'Ingénieur - Environnement. <https://doi.org/10.51257/a-v1-g1750>
- [25] Razi, N., Svendsen, H.F., Bolland, O., 2014. Assessment of mass transfer correlations in rate-based modeling of a large-scale CO₂ capture with MEA. *Int. J. Greenh. Gas Con.* 26, 93–108. <https://doi.org/10.1016/j.ijggc.2014.04.019>
- [26] Cho, J.S., Wakao, N., 1988. Determination of liquid-side and gas-side volumetric mass transfer coefficients in a bubble column. *J. Chem. Eng. Japan* 21, 576–581. <https://doi.org/10.1252/jcej.21.576>
- [27] Colombet, D., Legendre, D., Cockx, A., Guiraud, P., 2013. Mass or heat transfer inside a spherical gas bubble at low to moderate Reynolds number. *Int. J. Heat Mass Transf.* 67, 1096–1105. <https://doi.org/10.1016/j.ijheatmasstransfer.2013.08.069>
- [28] Shao, N., Gavriilidis, A., Angeli, P., 2010. Mass transfer during Taylor flow in microchannels with and without chemical reaction. *Chem. Eng. J.* 160, 873–881. <https://doi.org/10.1016/j.cej.2010.02.049>
- [29] Sobieszuk, P., Ilnicki, F., Pohorecki, R., 2014. Contribution of liquid- and gas-side mass transfer coefficients to overall mass transfer coefficient in Taylor flow in a microreactor. *Chem. Process Eng.* 35, 35–45. <https://doi.org/10.2478/cpe-2014-0003>
- [30] Polák, J., Mertl, I., 1965. Saturated vapour pressure of methyl acetate, ethyl acetate, n-propyl acetate, methyl propionate, and ethyl propionate. *Collect. Czechoslov. Chem. Commun.* 30, 3526–3528. <https://doi.org/10.1135/ccccc19653526>
- [31] Warnier, M.J.F., de Croon, M.H.J.M., Rebrov, E.V., Schouten, J.C., 2010. Pressure drop of gas–liquid Taylor flow in round micro-capillaries for low to intermediate Reynolds numbers. *Microfluid. Nanofluidics* 8, 33. <https://doi.org/10.1007/s10404-009-0448-z>
- [32] Bretherton, F.P., 1961. The motion of long bubbles in tubes. *J. Fluid Mech.* 10, 166. <https://doi.org/10.1017/S0022112061000160>
- [33] Aussillous, P., Quéré, D., 2000. Quick deposition of a fluid on the wall of a tube. *Phys. Fluids* 12, 2367. <https://doi.org/10.1063/1.1289396>
- [34] Durán-Martínez, F.L., Julcour, C., Billet, A.-M., Larachi, F., 2016. Modelling and simulations of a monolith reactor for three-phase hydrogenation reactions — Rules and recommendations for mass transfer analysis. *Catal. Today* 273, 121–130. <https://doi.org/10.1016/j.cattod.2016.04.009>
- [35] Albrand, P., Julcour, C., Billet, A.-M., 2021. Sunflower hydrogenation in Taylor flow conditions: Experiments and computational fluid dynamics modeling using a moving mesh approach. *Ind. Eng. Chem. Res.* 60, 16701–16719. <https://doi.org/10.1021/acs.iecr.1c02801>
- [36] Fukagata, K., Kasagi, N., Ua-arayaporn, P., Himeno, T., 2007. Numerical simulation of gas–liquid two-phase flow and convective heat transfer in a micro tube. *Int. J. Heat Fluid Fl.* 28, 72–82. <https://doi.org/10.1016/j.ijheatfluidflow.2006.04.010>
- [37] Gupta, R., Fletcher, D.F., Haynes, B.S., 2010. Taylor flow in microchannels: A review of experimental and computational work. *J. Comput. Multiph. Flows* 2, 1–31. <https://doi.org/10.1260/1757-482X.2.1.1>

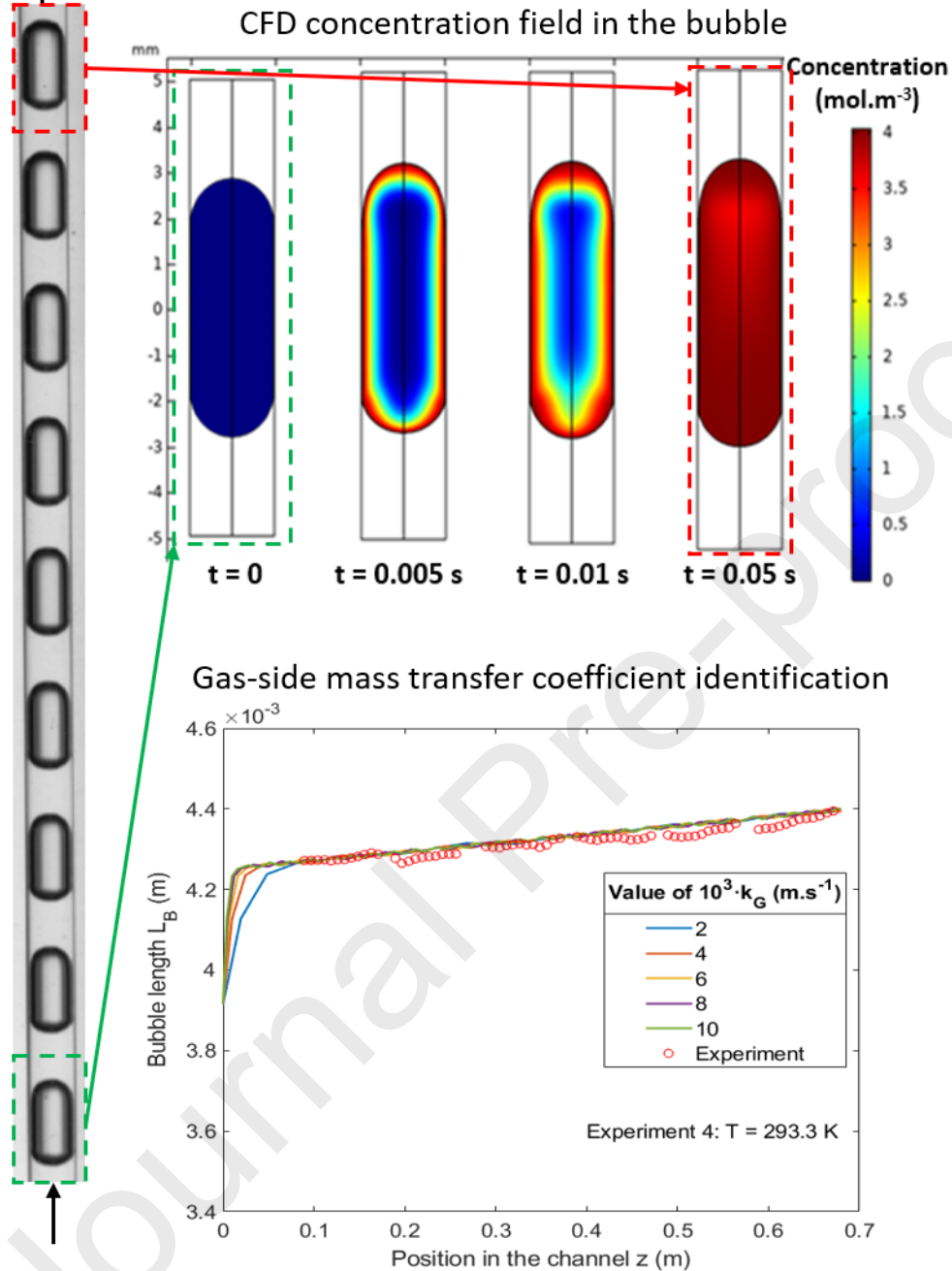
- [38] Albrand, P., Julcour, C., Gerbaud, V., Billet, A.-M., 2020. Accurate hydrogenated vegetable oil viscosity predictions for monolith reactor simulations. *Chemical Engineering Science*, Chem. Eng. Sc. 214, 115388. <https://doi.org/10.1016/j.ces.2019.115388>
- [39] Triplett, K.A., Ghiaasiaan, S.M., Abdel-Khalik, S.I., Sadowski, D.L., 1999. Ga-liquid two-phase flow in microchannels Part I : two-phase flow patterns. *Int. J. Multiph. Flow* 18. [https://doi.org/S0301-9322\(98\)00054-8](https://doi.org/S0301-9322(98)00054-8)
- [40] Fuller, E.N., Schettler, P.D., Giddings, J. Calvin., 1966. New method for prediction of binary gas-phase diffusion coefficients. *Ind. Eng. Chem.* 58, 18–27. <https://doi.org/10.1021/ie50677a007>
- [41] Butler, C., Cid, E., Billet, A.-M., Lalanne, B., 2021. Numerical simulation of mass transfer dynamics in Taylor flows. *Int. J. Heat Mass Transf.* 179, 121670. <https://doi.org/10.1016/j.ijheatmasstransfer.2021.121670>
- [42] Ellis, C.S., Holsen, J.N., 1969. Diffusion coefficients for helium-nitrogen and nitrogen-carbon dioxide at elevated temperatures. *Ind. Eng. Chem. Fund.* 8, 787–791. <https://doi.org/10.1021/i160032a030>
- [43] Rinker, E.B., Sami, S.A., Sandall, O.C., 1995. Kinetics and modelling of carbon dioxide absorption into aqueous solutions of N-methyldiethanolamine. *Chem. Eng. Sc.* 50, 755–768. [https://doi.org/10.1016/0009-2509\(94\)00444-V](https://doi.org/10.1016/0009-2509(94)00444-V)
- [44] Vandu, C.O., Liu, H., Krishna, R., 2005. Mass transfer from Taylor bubbles rising in single capillaries. *Chem. Eng. Sc.* 60, 6430–6437. <https://doi.org/10.1016/j.ces.2005.01.037>

Sample CRediT author statement

Emilien Bourdon: Conceptualization, Methodology, Investigation, Software, Writing – Original Draft. **Carine Julcour:** Conceptualization, Methodology, Software, Supervision, Writing – Review & Editing. **Anne-Marie Billet:** Conceptualization, Methodology, Supervision, Writing – Original Draft. **David Rouzineau:** Methodology, Supervision, Writing – Review & Editing. **Céline Volpi:** Supervision, Project administration, Resources, Writing – Review & Editing. **Renaud Cadours:** Conceptualization, Methodology, Supervision, Writing – Review & Editing.

Graphical abstract

Evaporation of pure solvent in Taylor flow: Gas-side mass transfer study



Highlights

- Local mass transfer in gas-liquid upward Taylor flow studied by shadowgraphy method
- Evaporation of ethyl acetate into nitrogen flow to evaluate gas-side coefficient k_G
- Bubble length evolution described by a model including mass transfer & pressure drop
- Direct numerical simulation of solvent vaporization including Taylor bubble expansion
- Study of temperature, two-phase velocity & gas diffusivity effects on k_G

Declaration of interests

The authors declare that they have no known competing financial interests or personal relationships that could have appeared to influence the work reported in this paper.

The authors declare the following financial interests/personal relationships which may be considered as potential competing interests:

Journal Pre-proofs